Dynamics of Shear-Induced Alignment of a Lamellar Diblock: A Rheo-optical, Electron Microscopy, and X-ray Scattering Study

Z.-R. Chen, A. M. Issaian, and J. A. Kornfield*

Chemical Engineering 210-41, California Institute of Technology, Pasadena, California 91125

S. D. Smith, J. T. Grothaus, and M. M. Satkowski

Procter & Gamble, Cincinnati, Ohio 45239

Received May 13, 1997; Revised Manuscript Received September 2, 1997[⊗]

ABSTRACT: In-situ rheo-optical methods are used to guide electron microscopy (TEM) and X-ray scattering (SAXS) studies of structure development during flow-induced alignment in a lamellar block copolymer melt (nearly symmetric polystyrene−polyisoprene diblock, ODT ≃ 172 °C). The progress of shear-induced alignment is recorded in real-time using flow birefringence; at selected points during alignment samples are taken for ex-situ characterization by TEM and SAXS along all three axes (**v**, ∇**v**, ∇ × **v**) of the flow geometry. Three different trajectories are examined: perpendicular alignment and two qualitatively different routes to parallel alignment in the high-frequency regime ($\omega > \omega_c'$). In general, the initial "fast" process not only enhances the projection of the orientation distribution that corresponds to the final state but also increases other projections of the distribution; the late-stage "slow" process eliminates these other projections and perfects a single alignment. For example, the highest frequency path to parallel alignment begins by transforming poorly organized regions into layers that are predominantly oriented along the parallel and transverse directions. The transition to the slow process is marked by the development of a characteristic texture in which tilt wall boundaries normal to the flow direction separate bands that form a repeating "chevron" pattern (layers tilted up and down about the ∇×**v** axis). The coarsening of this pattern dominates the slow process, during which the transverse projection is also eliminated.

1. Introduction

Driven by the increasing interest in nanotechnology, materials that spontaneously form nanometer scale ordered structures are attracting intense attention. These systems may prove useful if their ordered structures can be used to pattern surfaces or produce materials in which the nanostructure extends to macroscopic scales. Block copolymers represent an important class of nanostructured materials because their morphology and dynamics can be systematically controlled by choice of the polymer segments and their relative length. Under the influence of applied fields, their ordered structure can be aligned to produce "single-crystal-like" materials, which has inspired extensive investigation of flow- and electric-field-induced alignment in block copolymers.[1−32] Since the discovery that large amplitude oscillatory shear at different frequencies could produce either "parallel" or "perpendicular" alignment (Figure 1),[7,8] there has been particularly keen interest in the mechanism of selection of one orientation over the other. However, fundamental understanding of the mechanisms and dynamics of alignment remains elusive.

In situ, time-resolved experiments are revealing the richness of the structural evolution that can occur during flow-induced alignment of ordered block copolymers.[8,14,17−19,25−28,30] For example, in situ X-ray scattering studies by Hashimoto and co-workers showed that shearing a lamellar block copolymer melt can produce bimodal orientation distributions with parallel and transverse populations.[30] And in-situ neutron scattering measurements have shown that prolonged shearing can move lamellar block copolymer solutions through a predominantly perpendicular aligned state to a weakly ordered state with preferential parallel orientation.[28] These scattering studies have achieved a time resolution of a few minutes. Transient birefringence measurements provide an effective means to monitor faster alignment processes with a time resolution of a few milliseconds.[14,17−19] The speed of these methods has proved useful in characterizing the rapid changes that occur in the early stages of the alignment process and for examining the effects of processing parameters on the rate and degree of alignment.

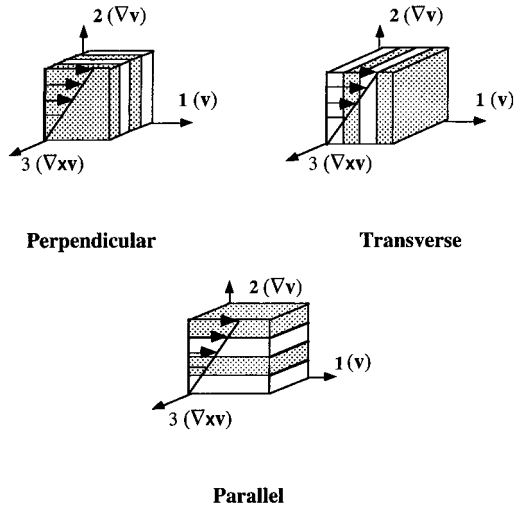

Figure 1. Schematic diagram of the three principal lamellar orientations: (a) perpendicular; (b) transverse; (c) parallel.

Three regimes of behavior in the present lamellar PS−PI have been distinguished on the basis of their rheo-optical signatures (Figure 2): the perpendicular regime previously identified in similar PS−PI diblocks and two distinct pathways to parallel alignment within the high-frequency regime where parallel alignment had previously been observed. The body of in-situ results indicates a complex interplay of temperature, shearing

[⊗] Abstract published in *Advance ACS Abstracts,* October 15, 1997.

S0024-9297(97)00674-8 CCC: $14.00

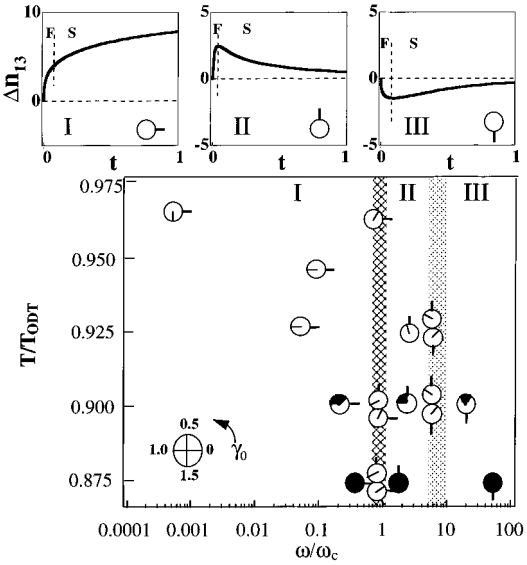

Figure 2. Three families of alignment trajectories are observed for PS−PI lamellae that have been heated through the ODT to erase their thermal and flow history and then cooled to a particular temperature in the ordered state where flow-induced alignment is performed: (I) perpendicular alignment at $\omega < \omega_c'$; (II) parallel alignment at frequencies above, but close to, ω_c'; (III) parallel alignment at $\omega \gg \omega_c'$. Each regime has a qualitatively different signature in the transient 1,3-birefringence during alignment (top row). The range of temperatures, frequencies, and strain amplitudes over which each type of alignment trajectory is observed is represented on a three-dimensional plot,[19] where the third dimension of strain is indicated inside the open symbols (see dial in the lower left of the graph). Filled symbols show the conditions used in the present study (see Figures 5a, 9a, and 14a for range of strain amplitudes). Conditions shown lead to a well-aligned state (see text) in less than 10 h. Two symbols directly atop one another represent different alignments or trajectories at identical temperatures and frequencies, but different strain amplitude.

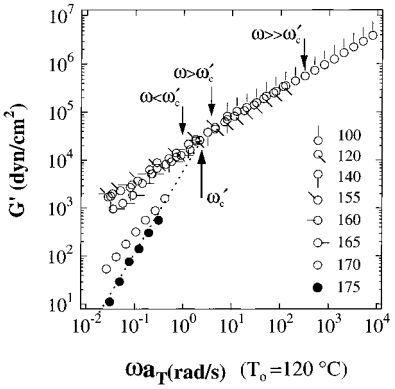

Figure 3. Storage modulus of the disordered and ordered, unaligned states for the present PS−PI diblock. Although the disordered state results lie in the terminal regime for all experimentally accessible frequencies, the critical frequency ω_c' can be estimated by comparison to materials for which the disordered and ordered state data converge. The arrows above the data points indicate the reduced frequencies that are used for the shear-induced alignment experiments and are labeled according to the flow alignment regime to which they belong (see text).

frequency, and strain amplitude in controlling the changes in the state of order and orientation during shearing. These have been summarized in a three-dimensional mapping of alignment behavior as a function of T/T_{ODT}, ω/ω_c', and γ_o (Figure 2),[19] where T_{ODT} is the order−disorder transition temperature, ω_c' is the frequency below which the ordered structure dominates the viscoelasticity of the material (Figure 3), and γ_o is the strain amplitude of the sinusoidal shear.

Rheo-optical studies have shown that all three of these families of alignment trajectories start with a "fast" process (marked "F" in Figure 2, top) that transforms the initial isotropic orientation distribution to an anisotropic distribution, followed by a later "slow" process (marked "S" in Figure 2, top) that eliminates all but one orientation, either parallel or perpendicular.[18,19] While these processes may be partially overlapping, they differ in time scale by over an order of magnitude, as well as showing pronounced differences in the strain dependence of their respective rates.[19] The fast process of trajectories to perpendicular alignment and to parallel alignment at $\omega_c' < \omega < 10\omega_c'$ produces an orientation distribution with a mix of perpendicular and parallel projections, but little transverse projection (positive Δn_{13}, Figure 2, top, I and II). However, at very high shear frequencies, the nature of the fast process changes and produces an orientation distribution that consists of a mix of transverse and parallel projections (negative Δn_{13}, Figure 2, top, III).

Now that distinct families of alignment pathways have been identified, the next step is to determine the nature of the fast and slow processes for each type of trajectory toward the goal of fundamentally understanding the effects of macromolecular design and processing parameters on the alignment behavior.

Ex-situ characterization methods have provided the majority of the structural information on flow-induced alignment.[1−3,7−12,15,16,24,29] Samples cooled and removed for characterization are amenable to TEM imaging and to SAXS or SANS studies in which the orientation distribution can be probed along each of the axes of the flow geometry. As a recent example, TEM imaging has revealed that samples with a bimodal parallel-transverse orientation distribution[20−22,29,30] can contain a striking banded texture with large regions of the predominant parallel orientation punctuated by bands of transverse lamellae sandwiched between parallel tilt-wall boundaries.[20] Alternatively, this type of orientation distribution can correspond to islands of transverse orientation embedded in a matrix of parallel-aligned material.[21] There is no in-situ method that can replace direct imaging of the nano- and microstructure. Ex-situ scattering along all three directions (**v**, ∇**v**, $\nabla\times$**v**) provided the basis for the original identification of parallel and perpendicular alignment.[7] More recently, this approach has clarified the evolution of structure during parallel alignment at very high frequencies (type III),[22,41] showing that the orientation distribution passes through a transient state characterized by a bimodal orientation distribution with coexisting parallel and transverse lamellae.

The detailed information gained by ex-situ characterization of texture (using TEM) and the orientation distribution (by SAXS or SANS) could provide insight into the nature of the distinct families of alignment trajectories, including their individual fast and slow processes. To establish the connection between structural changes and these individual processes, however, it is necessary to remove samples at known points in an overall alignment trajectory. To do so, one must have some in-situ probe of the progress of alignment in real time.

In this paper, we present such a detailed characterization of the evolution of microstructure during shear-induced alignment. We use in-situ birefringence measurements to identify selected points in the fast and slow processes and at the transition between them. Shearing is interrupted at the desired points and the

inevitable relaxation of the structure upon cessation of flow is recorded before the samples are cooled and removed for ex-situ studies using TEM and SAXS. This approach is applied to each of the three families of alignment pathways for PS−PI described by Gupta et al.[18,19] Following a brief description of the material and methods (section 2), we present the structural changes that are observed by TEM and SAXS for the fast and slow processes in each of the three regimes (section 3). Then we discuss the implications of these structural changes for the nature of alignment processes, examining existing concepts regarding alignment mechanisms and highlighting new insights that arise from the results.

2. Experimental Section

Materials. We used a nearly symmetric polystyrene−polyisoprene diblock copolymer with $M_w \simeq 20$ kg/mol, and $M_w/M_n \leq 1.06$.[33] Rheological determination of the order−disorder transition temperature indicated $T_{ODT} \simeq 172$ °C.[34] The viscoelastic spectra for the present PS−PI material in the disordered state and the ordered, but unaligned state (Figure 3) are in accord with those reported in Gupta et al.[18] The frequency (ω_c') associated with a crossover in the relaxation dynamics from being dominated by the macromolecular response to being dominated by the microstructural response is estimated to be $\omega_c' \approx 5$ rad/s at 120 °C (corresponding to $\omega_c' \approx 2$ rad/s at 115 °C). At shear frequencies above ω_c', parallel alignment is induced by prolonged sinusoidal shear of sufficiently large amplitude; at lower frequencies perpendicular alignment is induced.[18] The high-frequency regime ($\omega > \omega_c'$) of parallel alignment consists of two regions in terms of the pathway that leads to the aligned state, as described above.

Optical Rheometry. Simultaneous, quantitative measurements of dynamic stress and birefringence were performed on a Rheometrics RSA II modified for rheo-optical measurements. Experimental details have been presented earlier.[35] Light propagating along the velocity gradient direction (axis 2) is used to probe the projection of the refractive index tensor in the plane formed by the flow direction (axis 1) and the vorticity axis (axis 3), i.e., $\Delta n_{13} = n_{11} - n_{33}$. For PS−PI diblocks, the birefringence is dominated by the form contribution resulting from the microphase-separated structure.[36−38] Therefore, the evolution of the steady offset in $\Delta n_{13}^{(d)}(t)$ probes the orientation distribution of the lamellae (the 1,3-projection of the second moment tensor, as described in the Appendix of ref 19).

Perpendicular alignment, with the lamellar normal ($\hat{\mathbf{u}}$) along the neutral direction ($\hat{\mathbf{u}} \parallel$ axis 3), corresponds to positive $\Delta n_{13}^{(d)}$ for PS−PI, since the form contribution has a higher index along the layers. For an orientation distribution biased along the transverse direction ($\hat{\mathbf{u}} \parallel$ axis 1) relative to the perpendicular direction, the 1,3-birefringence is negative. In the parallel orientation ($\hat{\mathbf{u}} \parallel$ axis 2), the lamellae are normal to the beam propagation direction (Figure 1), resulting in zero birefringence in the 1,3-plane for a perfectly aligned parallel state. While a final large, positive value of 1,3-birefringence unambiguously reflects predominant perpendicular alignment, many states can give a final $\Delta n_{13}^{(d)}$ near zero. Therefore, final states with low $\Delta n_{13}^{(d)}$ have been interpreted in combination with the changes in the small strain dynamic moduli (G', G'') and the SAXS patterns observed in samples removed at the end of the process;[18,19] the resulting identification of parallel final states agreed with earlier structural studies using TEM and SAXS for a very similar polymer system.[9]

Shear-Induced Alignment and Preparation of Samples for Ex-Situ Characterization. Shear alignment experiments have been performed using prolonged, large amplitude oscillatory shear (LAOS). Here and in our previous studies[18,19] the shearing is sinusoidal (rather than reciprocating). Before each alignment experiment, the sample is heated well into the disordered phase (180 °C) and is allowed to equilibrate for 15−20 min to erase its previous thermal and deformation history. It is then cooled to the desired temperature in the ordered state and equilibrated for 15 min.[39] This procedure results in a reproducible initial condition, as confirmed by frequency sweep measurements using small strains. To examine the structure present in this initial state, a sample was taken through the protocol above and then cooled to ambient temperature and removed from the cell without subjecting it to any shearing.

A temperature of 115 °C was chosen for the present experiments; three frequencies were chosen that lie in each of the three alignment regimes shown in Figure 2. The selected conditions are represented by the solid symbols in Figure 2 and by the arrows in Figure 3. The birefringence trajectories for each regime form a family of alignment transients as a function of strain: above a critical strain, a well-aligned state can be reached and the rate of the alignment process generally increases strongly with increasing strain amplitude (below the critical strain characteristic of a given temperature and frequency the system progresses to an anisotropic structure but then fails to evolve to a fully oriented one). The present experiments are conducted far enough from the boundaries between regimes that we can neglect the more complex effects of strain: at the boundary between the perpendicular and parallel regimes (I and II, Figure 2), strain can flip the direction of alignment,[17] and in the boundary region between the two parallel alignment regimes II and III (Figure 2), strain amplitude can change the character of the alignment trajectory from one to the other.[19]

From each family of alignment trajectories we choose one for which the fast process is slow enough for us to reliably interrupt this process at a desired point. Along each of the three trajectories (one per regime), three points are chosen that represent roughly (A) the midpoint in the fast process, (B) the transition between the fast and slow processes, and (C) the midpoint of the slow process. We do not show the characterization of the final well-aligned state here since the SAXS results for each case have been published previously[19] and the TEM images are so uniform that they are essentially featureless over large length scales in samples removed when the birefringence indicates the alignment process is complete. Ten samples were used for the TEM and SAXS measurements, representing the initial, unaligned state and points A, B, and C for three different trajectories (all at $T = 115$ °C: $\omega = 1$, 4, and 100 rad/s with $\gamma_o = 0.6$, 0.7, and 0.3, respectively).

It is worth noting that the ex-situ experiments are subject to complications that are not present in our previous suite of rheo-optical experiments: variations in the samples[33] and in the temperature controller, uncertainties in the precise flow cell geometry, and possible distortion of the aligned structure during cooling and unloading. For the SAXS experiments performed with the beam along either the flow or vorticity directions, effects of cutting the sample could affect the results. Similarly, sample preparation can affect TEM results and is combined with the challenge of examining enough material to ensure that representative images are selected for interpretation. These complications are present in all studies that use ex-situ methods. A sample preparation guided by rheo-optical methods does assist in assessing the extent of structural relaxation after cessation of shearing and during cooling to ambient temperature. While the absence of a change in optical anisotropy does not rule out changes in structure, large changes in optical anisotropy give a valuable warning sign that structural changes must have occurred during relaxation and cooling. This information can influence how strongly we interpret the ex-situ results as representing the structure that actually existed during the flow-induced alignment process.

Substantial relaxation was observed when the fast process was interrupted (Figures 5b, 9b, and 14b); this suggests that the states of the harvested samples for point A of each trajectory have relaxed partially back toward an isotropic distribution and retain a lower degree of alignment than existed at the corresponding point during the alignment process. A more modest relaxation occurred when shearing was interrupted in the transition between the fast and slow processes (point B) and negligible relaxation was observed when the slow process was interrupted (e.g., point C). Beyond the three conditions used to prepare the samples for ex-situ characterization, we evaluated the magnitude of relaxation observed upon cessation of shearing for a wide range of shear

frequency, strain amplitude, and shearing time. At the early stages of the fast process (approximately halfway to point A), the 1,3-birefringence can relax to as little as half its magnitude just prior to cessation of shearing. The magnitude of the relaxation rapidly decreases as one moves through the fast process; the behavior shown for points A and B in Figures 5b, 9b, and 14b is representative of the behavior found for many other alignment trajectories for each of the three families interrupted at times that were beyond the midpoint of the fast process. The relaxation processes typically take between 100 and 500 s.

The birefringence was also recorded during cooling from 115 °C to room temperature; these changes were small compared to the relaxation upon cessation of shearing for point A of each trajectory. After cooling to room temperature, the samples were carefully removed from the shear sandwich tools and collected for TEM and SAXS measurements.

Small Angle X-ray Scattering. X-ray scattering patterns were collected using a Siemens small angle scattering system that includes an Anton Paar HR-PHK high-resolution pinhole optics system with a multiwire 2-D X-ray detector. The generator was a Rigaku RU-300 rotating anode operated at 40 kV and 40 mA with a 0.2 mm × 2 mm filament set in the spot focus mode. The X-ray beam is collimated by a 100 μm diameter pinhole placed approximately 490 mm from the focal spot. Another pinhole 300 μm in diameter is set 650 mm from the focal spot. This second pinhole reduces the parasitic scattering from the first pinhole. The sample to detector distance is approximately 650 mm. This arrangement leads to an incident X-ray spot on the sample of a diameter about 0.2 mm. Samples are set on a micrometer holder that is adjusted to place the sample such that the incident beam strikes the sample completely. All samples were in the range of 0.6−0.8 mm in thickness. X-ray patterns were collected for either 10 or 30 min. The patterns were normalized for differences in thickness and collection time. Background scattering was negligible (less than 1% of the signal in the peaks). In fact, background scattering amounted to less than 1 or 2 counts per pixel per 30 min except very near the beam stop. Therefore, background corrections were ignored in these qualitative runs.

Transmission Electron Microscopy. For TEM, material is taken from the center of the sample. Typically a 1 mm × 2 mm piece is cut from the middle of the slab of material removed from the flow cell. The sample is cut into a shape such that the orientation of each of the axes of the flow geometry ($\mathbf{v}$, $\nabla\mathbf{v}$, $\nabla\times\mathbf{v}$) is readily evident during specimen placement for microtoming. The sample is placed on the specimen carrier to achieve the desired orientation: for sections in the ($\mathbf{v}$, $\nabla\times\mathbf{v}$) or (1,3) plane, the sheet of material is glued flat onto the mounting stub; for sections in ($\mathbf{v}$, $\nabla\mathbf{v}$) = (1,2) or ($\nabla\mathbf{v}$, $\nabla\times\mathbf{v}$) = (2,3) planes, the sample is fastened to the stub edge-on using a sucrose solution. The chamber of the cryomicrotome (Reichert Ultra-cut S with Leica EM-FCS chamber) is held at a relatively low temperature of −160 °C so that the structures in the material will remain rigid and so that relatively thin (30−35 nm) sections can be obtained. Our trimming protocol produces an asymmetric, trapezoidal face that allows us to keep track of the orientation of the sections relative to the previous shearing geometry. First, we cut 100 μm into the sample to generate a clean face and avoid any surface artifacts. Then edges are cut on the right and left sides of the sample with a slight splay (5°) inward on each side; the parallel edges of the trapezoid are made by rotating the sample 90° and cutting straight edges (~25 μm) on each side. When the sample is rotated back, the long edge of the trapezoid is at the bottom and the shorter edge at the top. A Diatome diamond specimen trimmer is used for facing and trimming; a Micro Star Technologies 35° angle diamond knife is used for sectioning. Sections are cut with 30−35 nm thickness, typically using a 0.05 mm/s cutting speed. Sections are placed on 300 mesh, carbon-coated grids. Samples are stained by exposing them to the vapor over OsO_4 crystals for 40 min. Images are recorded using a Phillips 420 (120 keV) microscope. During an imaging session, the orientation of the trapezoidal section relative to the alignment of the frame of the photograph is noted for each exposure. These notes are used to draw the orientation of the axes onto the images after prints are made. The cumulative uncertainty in recording the orientation of the images is less than ±10°.

3. Results

Before describing the evolution of structure as alignment progresses, we first establish the initial condition that pertains to all three families of alignment trajectories. Then we describe the changes in microstructure and orientation distribution that occur along each of the three alignment trajectories in order of ascending frequency.

A. Initial Unaligned State. The unaligned sample was obtained by heating through the ODT to remove any effects of thermal history and prior deformation associated with molding and loading the sample and then cooling to the temperature used for all of the shear-induced alignment experiments, as described in the Experimental Section. It was imaged using sections taken in all three projections described above. No difference between the three directions was observed. The sample consists predominantly (roughly 70%) of poorly organized regions that have not formed well-defined layers (Figure 4).[39] These poorly organized areas may still be regarded as ordered in the sense that they show microphase segregation into styrene-rich and isoprene-rich domains on the same length scale that is observed in the well-organized regions. Layered domains also exist and show a variety of defect structures, including some that are reminiscent of partially formed focal conics. Scattering results show that the initial structure is essentially isotropic. A slight anisotropy is evident in the scattering pattern in the ($\nabla\mathbf{v}$, $\mathbf{v}$) plane. The orientation of this anisotropy does not coincide with any plausible surface-induced effect since it is at an oblique angle with respect to either parallel or perpendicular orientations (which could correspond to homogeneous or homeotropic surface alignment tendencies). Instead, we believe that this slight alignment could be induced during the procedure for removing the sample from the flow cell. In the interpretation of subsequent scattering patterns, we bear in mind that features of this magnitude could be artifacts caused simply by removing the sample from the flow cell.

B. Shear-Induced Alignment at $\omega < \omega_c'$: The Path to Perpendicular Orientation. To monitor structure evolution during the perpendicular alignment process, shearing experiments were done at ω =1 rad/s and T = 115 °C ($\omega \approx 0.5\omega_c'$, marked "$\omega < \omega_c'$" in Figure 3). A series of alignment experiments using different strain amplitudes was performed to confirm that the behavior at this reduced frequency corresponds to that previously established for families of perpendicular alignment trajectories in this regime.[19] The behavior of the effective dynamic modulus during shearing and the buildup of the 1,3-birefringence are in accord with previous results.[18,19] The effective storage modulus (G'_{eff}) shows a large drop upon the first cycle of LAOS, with the initial value of G'_{eff}(1 rad/s, γ_o) being approximately one-fourth as large as the linear storage modulus of the unaligned material $G'_{\text{unaligned}}$(1 rad/s); the effective storage modulus drops by roughly another factor of 4 during the alignment process.[40] The growth of the perpendicular projection of the orientation distribution is manifested in a monotonic increase in the 1,3-birefringence (Figure 5a). With increasing strain amplitude, the kinetics of alignment become more rapid; in particular, the time scale of the fast process decreases as γ_o^{-3}, as observed previously.[19] The largest birefringence we have ever observed for a perpendicular aligned

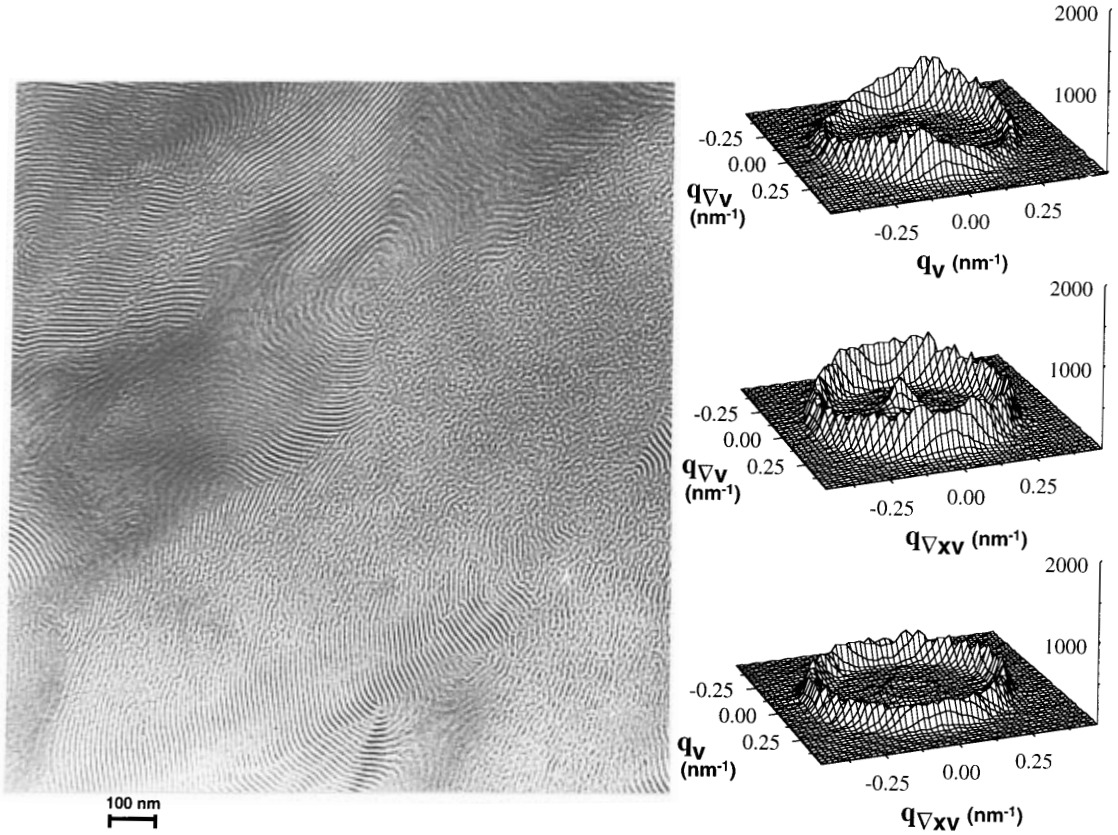

Figure 4. Structure of the initial condition as characterized by TEM and SAXS.

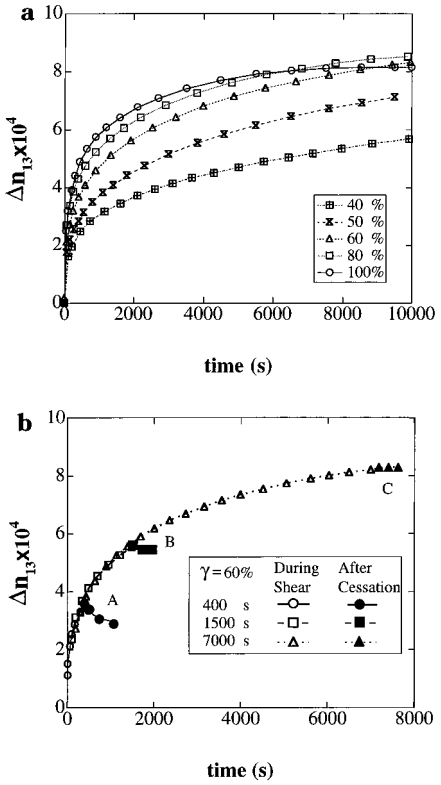

Figure 5. Development of perpendicular alignment driven by oscillatory shearing at $\omega = 1$ rad/s at $T = 115$ °C: (a) growth of the 1,3-birefringence with time during shearing with large strain amplitude ($\gamma_o \geq 0.4$); (b) birefringence during and upon cessation of shearing for samples prepared for ex-situ studies.

PS−PI is $\Delta n_{max} \simeq 1 \times 10^{-3}$;[19] in the time range reported here, the highest value reached is roughly 85% of this value, suggesting a high, but imperfect, degree of alignment.

For a trajectory that is representative of this whole family and affords a slow enough initial rise in the 1,3-birefringence to allow us to capture a sample in the middle of the fast process, we choose a strain amplitude of $\gamma_o = 0.6$ (Figure 5b). The samples harvested for ex-situ characterization were prepared by shearing for 400, 1500, and 7000 s at $\omega = 1$ rad/s and $\gamma_o = 0.6$, corresponding to 1,3-birefringence of 40%, 60%, and 80% of the highest value we have ever observed. These three points lie (A) in the fast process, (B) in the transition region between the fast and slow processes, and (C) in the middle of the slow process of the perpendicular alignment trajectory. By recording the birefringence and effective modulus during shearing, we confirmed that each of the three samples followed the same alignment dynamics as was established in the uninterrupted alignment experiment. Further, by recording the birefringence after cessation of shearing we gained information regarding potential differences in the structure of the static sample relative to the structure that existed in real-time during shearing (Figure 5b), as described in the Experimental Section.

Point A along the Perpendicular Alignment Trajectory. At approximately the midpoint in the fast process, the microstructure has a complex texture and an orientation distribution that is enriched in orientations that have their edges along the flow direction (Figure 6): parallel (indicated by the SAXS peaks in the (**v**, ∇**v**) plane), perpendicular (SAXS peaks in the (**v**, $\nabla\times$**v**) plane), and all orientations in between (nearly uniform ring of SAXS intensity in the (∇**v**, $\nabla\times$**v**) plane). In the TEM micrographs, the most noticeable change in microstructure with respect to the initial state is the increase in the proportion of material that is organized into layers. Images taken in the (**v**, ∇**v**) plane accord with an orientation distribution richer in parallel than transverse projections, as indicated by the correspond-

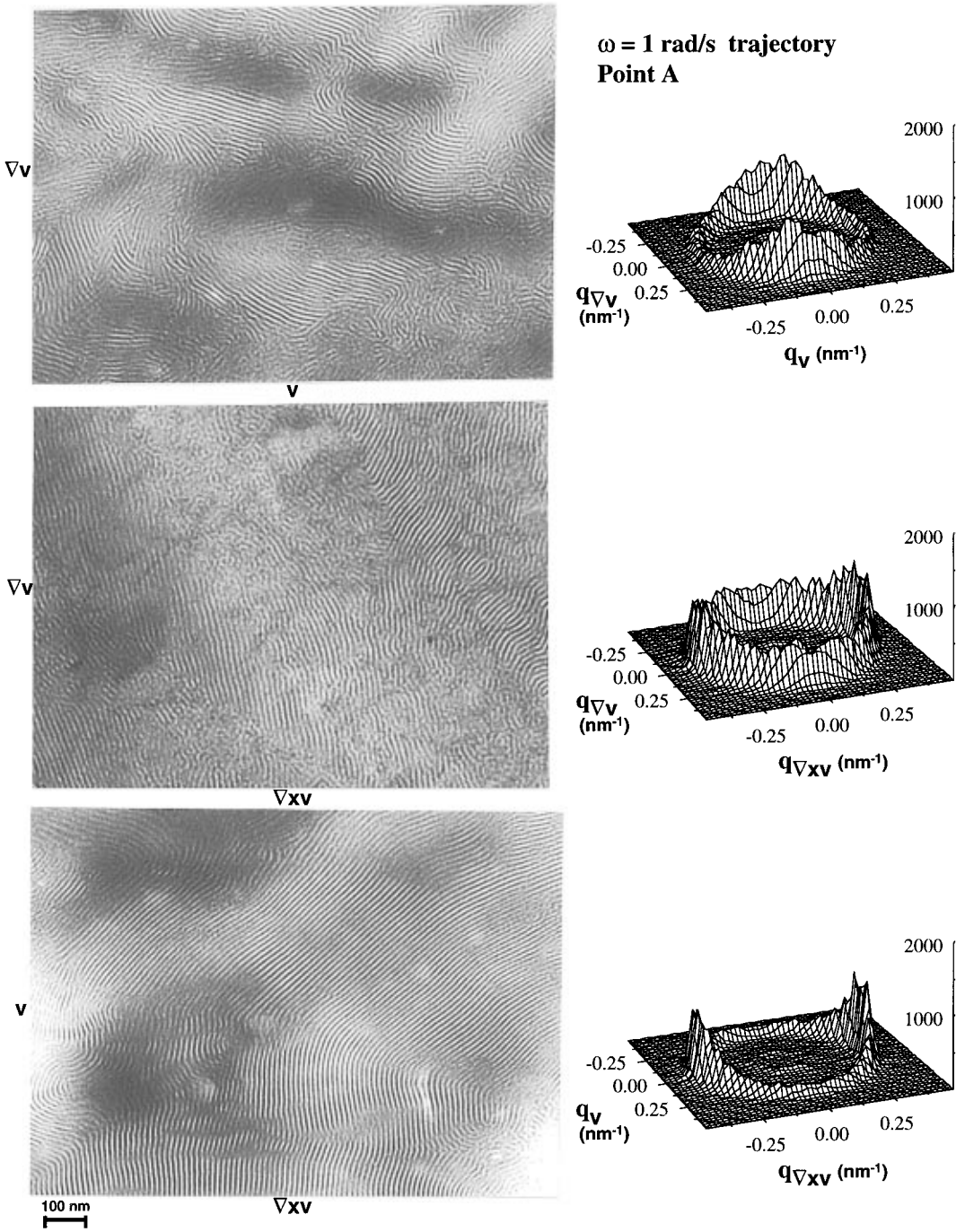

Figure 6. Structure at point A along the perpendicular alignment trajectory shown in Figure 5b as revealed by TEM and SAXS. The scale for SAXS intensity can be quantitatively compared to points B and C for this trajectory.

ing SAXS pattern; similarly, images in the (**v**, ∇×**v**) plane show a stronger projection of perpendicular than transverse layers, in agreement with both the SAXS and 1,3-birefringence results.

Point B along the Perpendicular Alignment Trajectory. At approximately the transition between the fast and slow processes, the orientation distribution shows a distinct enhancement of the perpendicular projection, as indicated by the increased intensity of the peaks in the SAXS pattern in the (∇**v**, ∇×**v**) plane (Figure 7). However, it is worth noting that the parallel projection is still present (the intensity of the peaks in the (**v**, ∇**v**) plane and of the ring of intensity in the (∇**v**, ∇×**v**) plane are similar at points B and A; they appear smaller in Figure 7 because the vertical scale has more than doubled). This type of scattering pattern has been reported in a similar system and interpreted as a final well-aligned state.[10] The TEM images also show the growth of the perpendicular population: in the (**v**, ∇**v**) plane regions with layers lying in that plane have developed, appearing uniform gray in the TEM image; in both the (∇**v**, ∇×**v**) and (**v**, ∇×**v**) planes there are many domains with layers perpendicular to ∇×**v**. Domain size has increased, especially along the velocity direction. Nevertheless, the texture is still riddled with defects and continues to contain some poorly organized regions (Figure 7).

Point C along the Perpendicular Alignment Trajectory. As the system evolves to the midpoint in the slow process, the perpendicular population continues to increase (stronger SAXS peaks in Figure 8 than in Figure 7), as indicated by the increase in 1,3-birefringence. The other projections that were enhanced during the fast process persist (peaks in the (**v**, ∇**v**) plane and of the ring of intensity in the (∇**v**, ∇×**v**) plane have only slightly decayed relative to points B and A; they appear

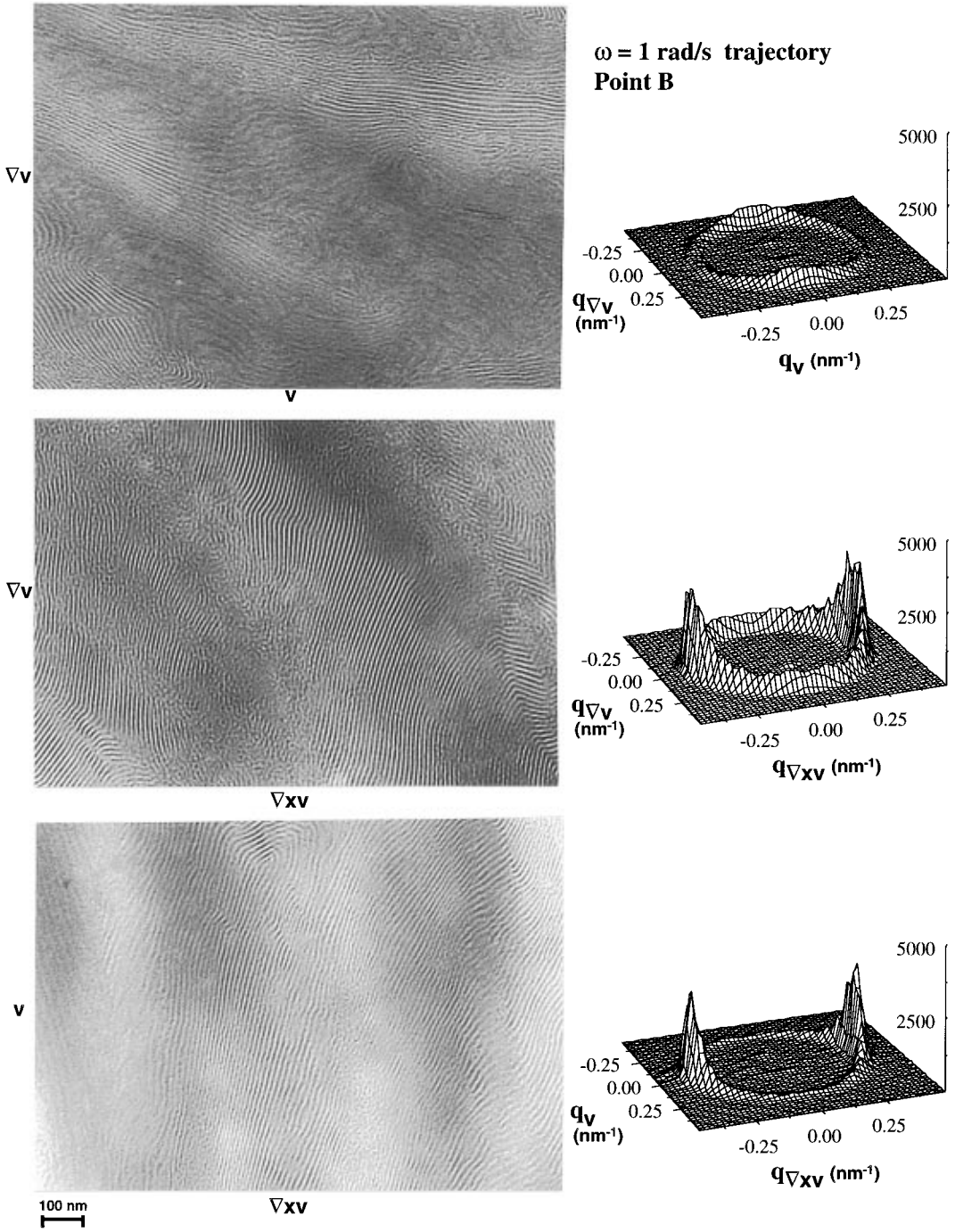

Figure 7. Structure at point B along the perpendicular alignment trajectory shown in Figure 5b as revealed by TEM and SAXS. The scale for SAXS intensity can be quantitatively compared to points A and C for this trajectory.

smaller because the peak intensity has doubled since point B). These projections are eliminated as the slow process reaches completion, indicated by their absence in the SAXS patterns of a perpendicular sample taken at the conclusion of the slow process.[19] The TEM results show that by the midpoint in the slow process virtually all of the material is organized into layers. The images in the (**v**, $\nabla\times$**v**) plane show a very high degree of alignment, in accord with the absence of a ring in the SAXS pattern for this projection. On the other hand, images in the (∇**v**, $\nabla\times$**v**) plane accord with a predominant alignment along the perpendicular orientation, but one that still contains many defects. The misalignments evident in TEM images in this plane accord with the presence of the ring of intensity in the corresponding SAXS pattern. The defects have a distinctive appearance dominated by undulations in orientation, rather than sharp kinks. The fact that these defects are seen in the (∇**v**, $\nabla\times$**v**) plane, but not in the (**v**, $\nabla\times$**v**) plane, indicate that they are anisotropic, with preferential alignment along the flow direction.

C. Shear-Induced Alignment at $\omega_c' < \omega < 10\omega_c'$: One Route to Parallel Orientation. Previous studies of lamellar PS−PI have shown that prolonged LAOS at frequencies above ω_c' induces parallel alignment.[9,10,15,18,19] Rheo-optical studies revealed that this high-frequency regime is actually composed of two regimes in terms of the *pathway* leading to the parallel alignment.[18,19] In this section we deal with the trajectories that pass through transient states with a higher population of the perpendicular rather than transverse orientation (suggesting transient distributions with strong parallel and perpendicular projections) that occur at frequencies above, but fairly close to ω_c'. The fol-

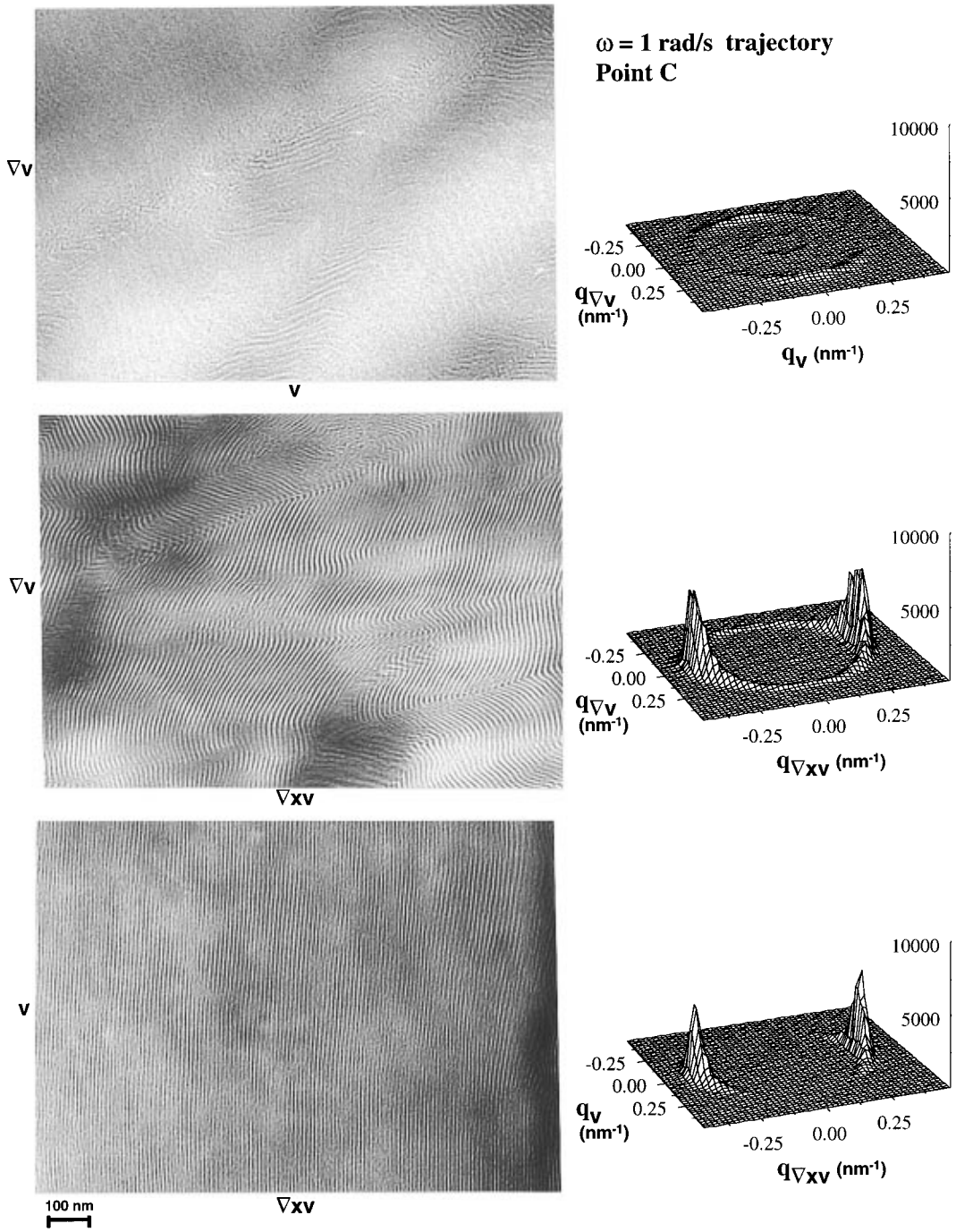

Figure 8. Structure at point C along the perpendicular alignment trajectory shown in Figure 5b as revealed by TEM and SAXS. The scale for SAXS intensity can be quantitatively compared to points A and B for this trajectory.

lowing section describes structure evolution along the trajectories to parallel alignment that pass through transient states with greater populations of transverse than perpendicular projections (suggesting transient states with strong parallel and transverse components) that occur at frequencies far above ω_c'.

Parallel alignment above but close to ω_c' was performed at $\omega = 4$ rad/s and $T = 115$ °C ($\omega \approx 2\omega_c'$, marked "$\omega > \omega_c'$" in Figure 3). A series of experiments using different strain amplitudes was done to confirm that the behavior at this reduced frequency corresponds to the established family of parallel alignment trajectories in this regime.[19] The effective storage modulus (G_{eff}') shows a modest drop immediately upon inception of LAOS, with the initial value of $G_{eff}'(4 \text{ rad/s}, \gamma_o)$ being approximately half the linear storage modulus of the unaligned material $G_{unaligned}'(4 \text{ rad/s})$; the effective storage modulus drops as much as an order of magnitude during the alignment process.[40] The time trace of the 1,3-birefringence indicates that in the early stages of the process a perpendicular projection grows stronger than the transverse projection of the orientation distribution, giving rise to a large positive birefringence (Figure 9a). The late stage of the process brings the 1,3-birefringence back to zero, which has previously been shown by SAXS to correspond to a well-aligned parallel final state.[19] Increasing strain amplitude speeds the kinetics of alignment, as observed previously.

As a representative trajectory from this family, we choose a strain amplitude of $\gamma_o = 0.7$ (Figure 9a). The samples harvested for ex-situ characterization were prepared by shearing for 22, 393, and 3121 s at $\omega = 4$ rad/s and $\gamma_o = 0.7$, corresponding to (A) the middle of the fast process, (B) the transition region between the

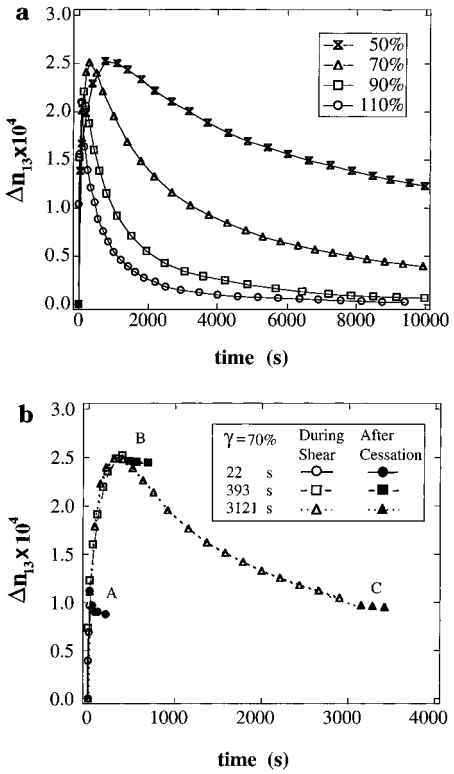

Figure 9. Development of parallel alignment driven by oscillatory shearing at $\omega = 4$ rad/s at $T = 115$ °C: (a) time evolution of the 1,3-birefringence during shearing with large strain amplitude ($\gamma_o \geq 0.5$); (b) birefringence during and upon cessation of shearing for samples prepared for ex-situ studies.

fast and slow processes, and (C) the middle of the slow process (Figure 9b). The birefringence and effective modulus observed during shearing confirmed that each of the three samples followed the same alignment dynamics as in an uninterrupted alignment experiment. The birefringence recorded after cessation of shearing was again used to monitor relaxation, as described in the Experimental Section.

Point A along the Parallel Alignment Trajectory above but near ω_c'. Moving from the initial condition to the midpoint of the fast process, there is an enhancement of the parallel projection (SAXS peaks in the ($\mathbf{v}$, $\nabla\mathbf{v}$) and ($\nabla\mathbf{v}$, $\nabla\times\mathbf{v}$) planes, Figure 10). The parallel layers coexist with projections of transverse (ring in the ($\mathbf{v}$, $\nabla\mathbf{v}$) plane SAXS) and perpendicular (ring in the ($\nabla\mathbf{v}$, $\nabla\times\mathbf{v}$) plane SAXS), but the perpendicular projection is the stronger of these (peaks in the ($\mathbf{v}$, $\nabla\times\mathbf{v}$) plane SAXS), as indicated by the sign of the 1,3-birefringence. Electron micrographs show that large regions remain poorly organized, although these have diminished relative to the initial condition. Examination of many images shows no clear preferred orientation.

Point B along the Parallel Alignment Trajectory above but near ω_c'. The parallel projection grows strongly and the transverse projection is eliminated as the system proceeds to the transition from the fast to slow processes (compare SAXS patterns in Figure 11 to Figure 10 to see the growth of the peaks and decay of the ring of intensity in the ($\nabla\mathbf{v}$, $\mathbf{v}$) plane, and the disappearance of the ring of intensity in the ($\mathbf{v}$, $\nabla\times\mathbf{v}$) plane). At the same time, the perpendicular projection has also grown stronger, giving the hint of a second set of peaks in the ($\nabla\mathbf{v}$, $\nabla\times\mathbf{v}$) plane and the growth of the peaks in the ($\mathbf{v}$, $\nabla\times\mathbf{v}$) plane. The increase in the perpendicular projection and the elimination of the transverse projection give rise to the increase in the 1,3-birefringence moving from point A to point B (Figure 9b). The texture revealed by TEM shows a distinct reduction in the fraction of material that is poorly organized. Many parallel aligned domains are observed in the images in the ($\nabla\mathbf{v}$, $\mathbf{v}$) plane. Electron micrographs in the ($\nabla\mathbf{v}$, $\nabla\times\mathbf{v}$) plane show a complex mix of parallel, perpendicular, and orientations between these two. Most of the field in the ($\mathbf{v}$, $\nabla\times\mathbf{v}$) plane appears featureless, indicative of parallel aligned regions; the regions that show lamellae edge-on tend to be close to the perpendicular alignment. All of these features of the TEM images accord well with the corresponding SAXS patterns.

Point C along the Parallel Alignment Trajectory above but near ω_c'. By the time the midpoint in the slow process is reached, a strong parallel alignment has developed. From point B to point C, the alignment of domains that were nearly parallel has significantly improved, leading to a 10-fold increase in the intensity of the peaks in the SAXS patterns in the ($\nabla\mathbf{v}$, $\mathbf{v}$) and ($\nabla\mathbf{v}$, $\nabla\times\mathbf{v}$) planes (Figure 12). On this scale, the slight projection of perpendicular layers that remains is imperceptible (negligible SAXS intensity in the ($\mathbf{v}$, $\nabla\times\mathbf{v}$) plane), in accord with the relatively small 1,3-birefringence that is left at point C. TEM images show parallel lamellae that are slightly undulating (see ($\nabla\mathbf{v}$, $\mathbf{v}$) and ($\nabla\mathbf{v}$, $\nabla\times\mathbf{v}$) images). Parallel lamellae are also indicated by the observation that over most of the sample the ($\mathbf{v}$, $\nabla\times\mathbf{v}$) sections are so featureless that it is difficult to focus the electron microscope; the image shown is not representative of the whole sample, since pictures were taken where features were available to use to focus the image.

Note that we do not regard the structure at the midpoint of the slow process as "well-aligned", a term we reserve for parallel states that have negligible 1,3-birefringence. The late stage of the shear alignment process eliminates the undulations from the lamellae, as manifested in sharper peaks in the SAXS patterns published earlier[19] and in the TEM micrographs of well-aligned parallel samples (Figure 13).

The early stages of this alignment trajectory may be related to the early stages of the flow process that leads to an initial enhancement of the perpendicular projection in reciprocating shear of a lamellar block copolymer solution.[28] The TEM image in the ($\nabla\mathbf{v}$, $\nabla\times\mathbf{v}$) plane of Figure 11 fits the description of undulations inferred from in-situ SANS results on a lamellar block copolymer solution[28] (although the undulations are not sharp enough to produce the previously reported splitting of the scattering peaks corresponding to the perpendicular population). However, the results of Wang et al. gave evidence of shear-induced disordering with time, whereas the present results suggest that the material remains ordered and becomes better and better organized into lamellae and progressively aligned in the parallel direction (Figures 10−12). Here we must be careful in comparing in-situ and ex-situ results due to the uncertainties inherent in ex-situ studies: substantial changes can occur between the cessation of shearing and the time a sample is removed for characterization. Fortunately, previous studies have shown that pronounced structural changes tend to require long times. For example, recovery of order after shear-induced disorder in solvated lamellae took over 40 min, even when the process was sped up by annealing at an elevated temperature relative to the shearing temperature.[28] And elimination of transverse bands in a primarily parallel biaxial texture of a lamellar diblock copolymer melt began on a time scale of 2 h at a temperature approximately 50 °C above T_g and was not complete after

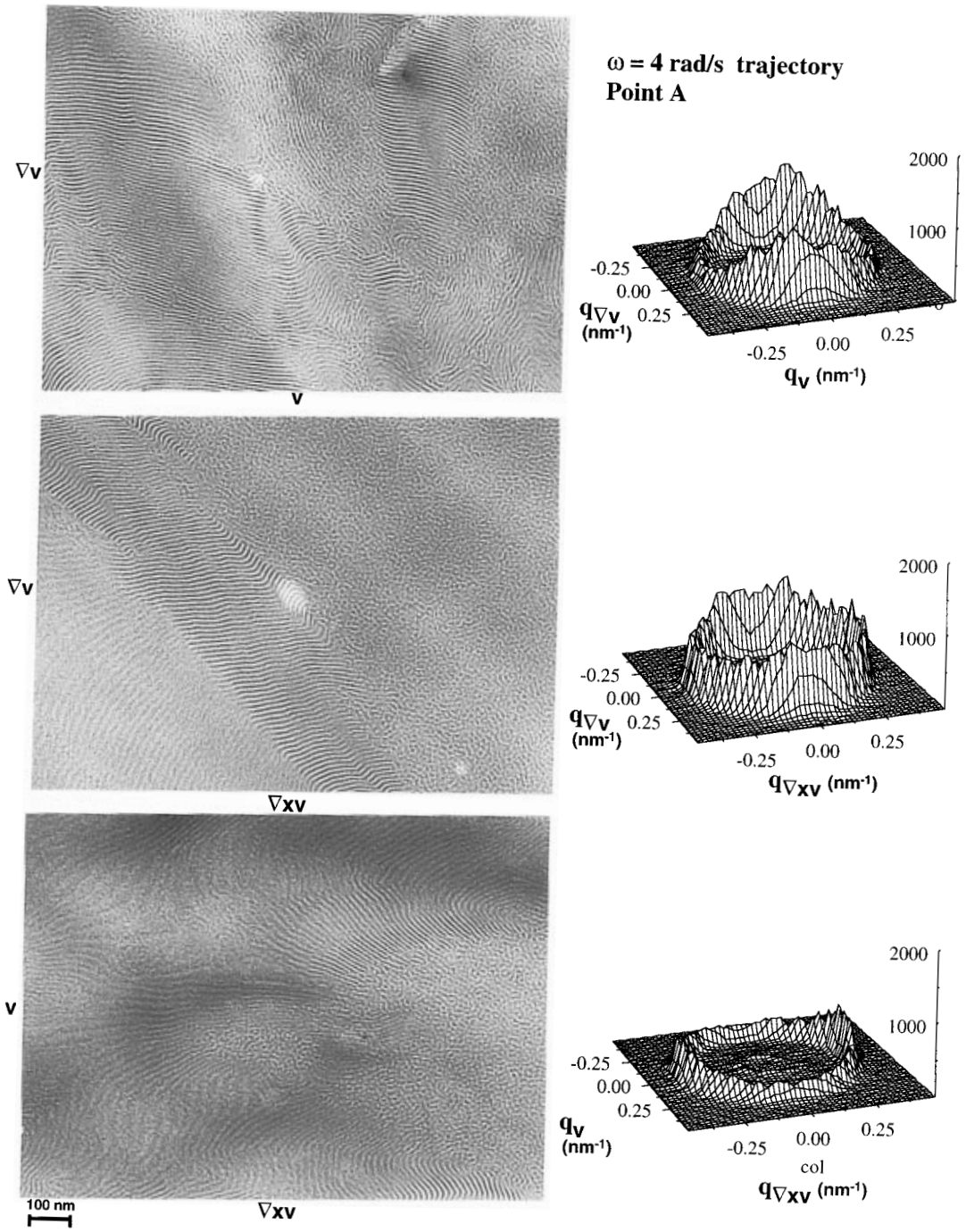

Figure 10. Structure at point A along the parallel alignment trajectory shown in Figure 9b as revealed by TEM and SAXS. The scale for SAXS intensity can be quantitatively compared to points B and C for this trajectory.

168 h.[20] The present samples were cooled through the glass transition after observing relaxations that occurred in the first few minutes after cessation of shearing, as described in the Experimental Section; this time scale is short compared to that required for the reorganizations reported previously during annealing after cessation of flow. Thus, the progressive improvement in lamellar order and alignment shown in these TEM images and SAXS patterns is probably a good reflection of the structural evolution in situ. This supports an interpretation of the type II birefringence trajectories in terms of progressive parallel alignment,[18,19] rather than progressive disordering.[28]

D. Shear-Induced Alignment at $\omega_c' \ll \omega$: Another Route to Parallel Orientation. The last family of trajectories we examine is the pathway to parallel alignment at frequencies far above ω_c'.[18,19] In this frequency regime, the orientation distribution evolves through transient states with stronger transverse than perpendicular projections on the way to parallel alignment. It has previously been inferred that the close correspondence between the time and strain dependence of the type III birefringence trajectories reported by Gupta et al.[18,19] and the series of "four-spot" SAXS patterns reported by Zhang and Wiesner[22] in this same frequency regime might indicate that an orientation distribution with distinct transverse and parallel populations gives rise to the negative 1,3-birefringence that is observed in this family of alignment trajectories.[19]

Parallel alignment at high shearing frequency ($\omega_c' \ll \omega$) was performed at $\omega = 100$ rad/s and $T = 115$ °C (corresponding to $\omega \approx 50\omega_c'$ shown by the arrow marked "$\omega \gg \omega_c'$" in Figure 3). The mechanical and optical signatures of these trajectories show that they

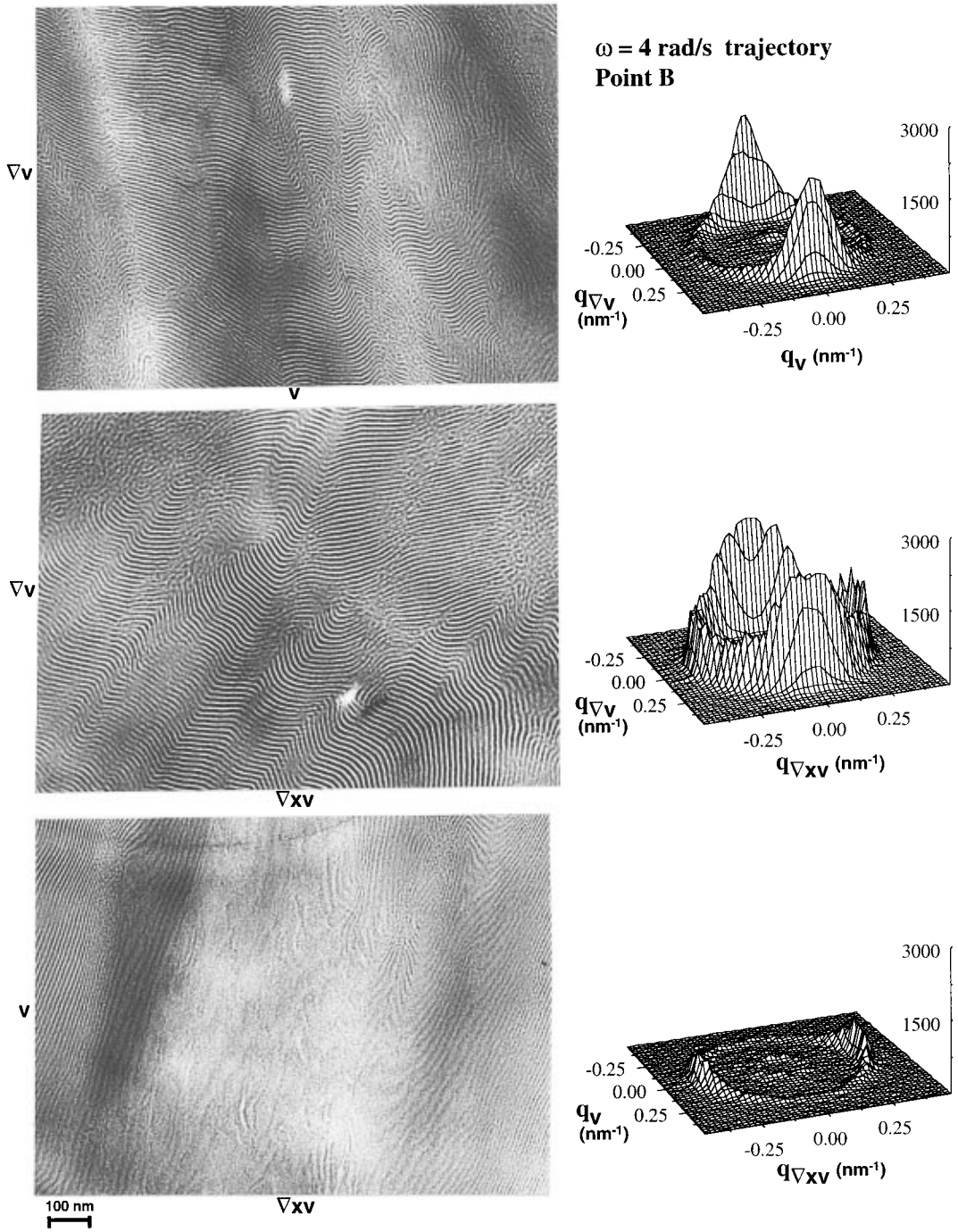

Figure 11. Structure at point B along the parallel alignment trajectory shown in Figure 9b as revealed by TEM and SAXS. The scale for SAXS intensity can be quantitatively compared to points A and C for this trajectory.

do belong to the high-frequency parallel alignment family reported previously by Gupta et al.[19] The initial drop in the effective storage modulus (G'_{eff}) upon inception of LAOS is relatively small compared to results at lower frequencies, with the initial value of G'_{eff}(100 rad/s, γ_o) being approximately 75% of the linear storage modulus of the unaligned material $G'_{unaligned}$(100 rad/s). The effective storage modulus drops as much as an order of magnitude during the alignment process, like the behavior for parallel alignment close to ω'_c.[40] It is interesting to note that the stress−strain behaviors during the two distinct parallel alignment processes are similar in spite of the dramatic differences between the two transient orientation distributions.[19] The 1,3-birefringence indicates that in the early stages of the process a *transverse* projection grows stronger than the perpendicular one, giving rise to a large *negative* birefringence (Figure 14a). The late stage of the process brings the 1,3-birefringence back to zero, which has previously been shown by SAXS to correspond to a final state that is well-aligned parallel.[19] The rate of the alignment process increases with strain amplitude, as observed previously.

The highest strain amplitude used in this series (γ_o = 0.7) is dictated by the onset of very subtle melt fracture. We find that at modestly higher strains ($\gamma_o \geq$ 0.8) the time dependence of the effective modulus changes: it undergoes an initial drop and flattening out but then enters a period in which the modulus gradually declines and does not plateau even after hours of shearing. At the same time the transmittance of the sample gradually declines. This behavior has proven to be an indicator that fissures will eventually develop in the sample, even though this macroscopic manifesta-

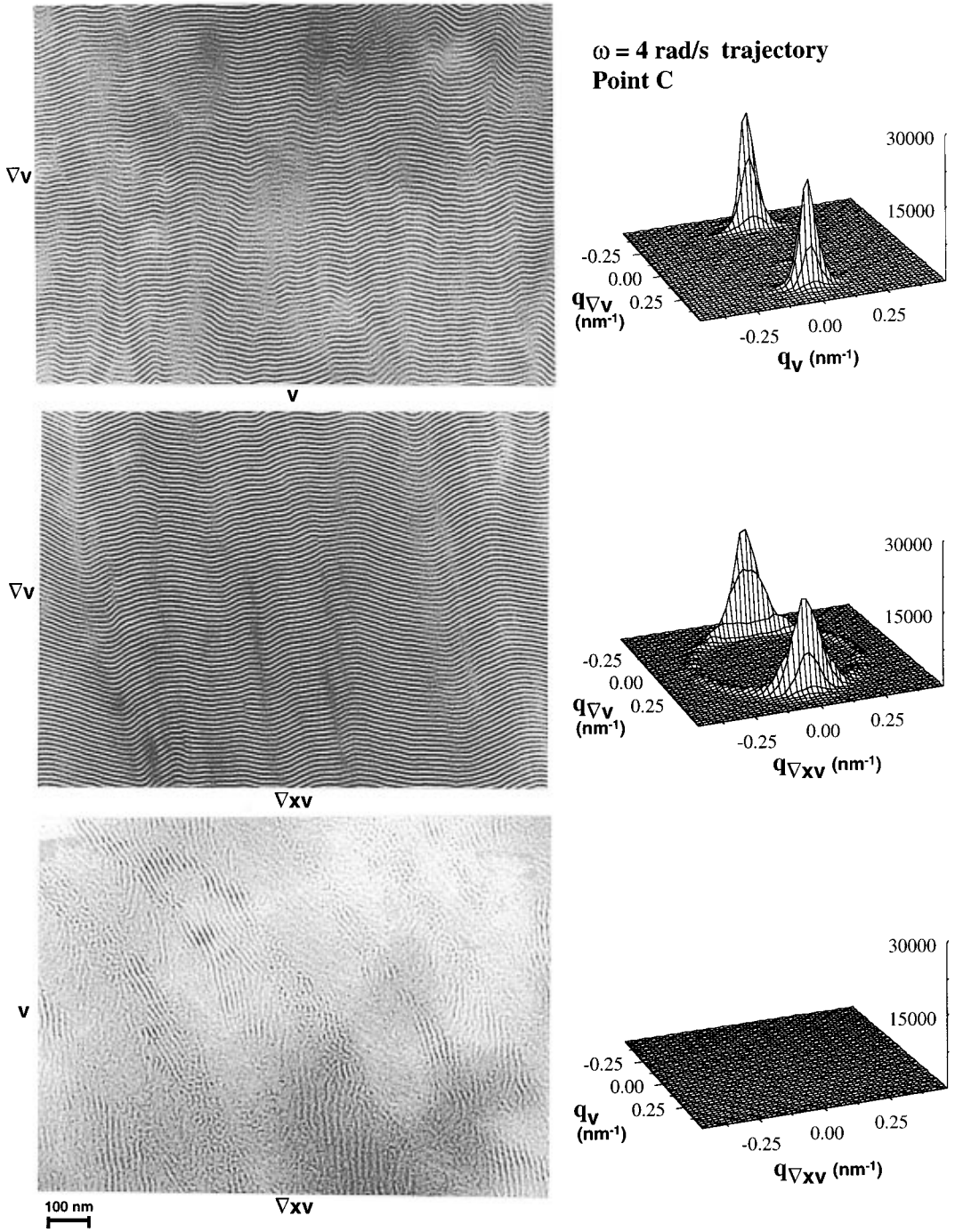

Figure 12. Structure at point C along the parallel alignment trajectory shown in Figure 9b as revealed by TEM and SAXS. The scale for SAXS intensity can be quantitatively compared to points A and B for this trajectory.

tion of melt fracture only occurs at much later times (many hours after the onset of the gradual decline of G_{eff}). If shearing is stopped prior to the formation of fissures, the linear modulus gradually increases with time. We believe that the effective modulus during shear and gradual recovery of G' after shearing reported by Pinheiro et al. may indicate the presence of this subtle form of incipient melt fracture.[29]

As a representative trajectory from this family that has a slow enough initial rise to allow us to capture a sample in the middle of the fast process, we use $\gamma_o = 0.3$ (Figure 14b). The samples harvested for ex-situ characterization were prepared by shearing for 137, 900, and 4900 s at $\omega = 100$ rad/s and $\gamma_o = 0.3$; as before, these points are selected because they lie in (A) the middle of the fast process, (B) the transition between the fast and slow processes, and (C) the middle of the slow process (Figure 14b). As previously, the birefringence and effective modulus recorded during the alignment process confirmed that each of the three samples followed the same dynamics as in an uninterrupted experiment. The birefringence observed during the relaxation after cessation of shearing (see Experimental Section) again indicated that appreciable relaxation only occurs when the fast process is interrupted. As in the preceding two cases, the birefringence recorded during cooling to room temperature did not indicate significant changes. After cooling to room temperature, the samples were collected for TEM and SAXS measurements.

Point A along the Parallel Alignment Trajectory Far above ω_c'. Between the initial condition and the midpoint in the fast process, a bimodal orientation distribution develops (Figure 15): a strong parallel component (indicated by the SAXS peaks in both the

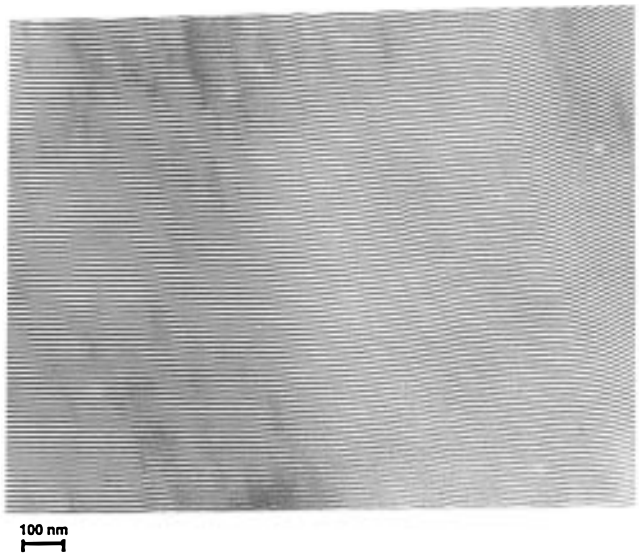

Figure 13. TEM image of a well-aligned parallel sample. Sample prepared by prolonged shearing at $T = 115$ °C, $\omega = 100$ rad/s, and $\gamma_o = 70\%$. This image is taken in the ($\nabla\mathbf{v}$, $\nabla\times\mathbf{v}$) plane. Although some defects do persist in this plane, large areas show uniform parallel alignment; in the ($\mathbf{v}$, $\nabla\mathbf{v}$) plane even fewer defects are observed.

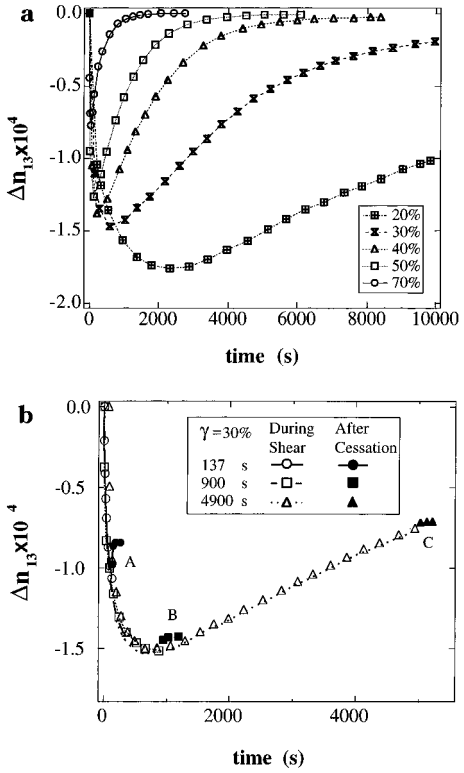

Figure 14. Development of parallel alignment driven by oscillatory shearing at $\omega = 100$ rad/s at $T = 115$ °C: (a) evolution of the 1,3-birefringence with time during shearing with large strain amplitude ($\gamma_o \geq 0.2$); (b) birefringence during and upon cessation of shearing for samples prepared for ex-situ studies.

($\nabla\mathbf{v}$, $\mathbf{v}$) and ($\nabla\mathbf{v}$, $\nabla\times\mathbf{v}$) planes) and a *transverse* component (SAXS peaks in both the ($\nabla\mathbf{v}$, $\mathbf{v}$) and ($\mathbf{v}$, $\nabla\times\mathbf{v}$) planes). The texture in the sample is quite complex, but it clearly shows a dramatic reduction in the amount of material that is in a poorly organized state (TEM images, Figure 15). In many domains the layers show good continuity, but in others the layers are discernible but perforated by many local defects on the scale of one or a few lamellae.

Point B along the Parallel Alignment Trajectory Far above ω_c'. Moving forward to the transition from the fast to the slow process, there is a dramatic growth in the parallel population and a slight increase in the transverse projection (see the intensities of the corresponding SAXS peaks in Figure 16 compared to Figure 15). The increase in the transverse component is in accord with the increasingly negative 1,3-birefringence developed between points A and B (Figure 14b). The microstructure in the sample shows extended domains in which the mean orientation is parallel, but the layers are tilted up and down in the velocity direction, making a "chevron" pattern when viewed down the vorticity axis (an example is shown in the left side of the TEM image in the ($\nabla\mathbf{v}$, $\mathbf{v}$) plane). This defect pattern is not seen in TEM images taken in the other two projections. Thus, the tilt walls are preferentially aligned normal to the flow direction. Electron micrographs show a distribution of tilt angles across the boundaries, in accord with seeing arcs of intensity in the ($\nabla\mathbf{v}$, $\mathbf{v}$) plane SAXS pattern along the $\nabla\mathbf{v}$ direction. In addition, there are domains in which the orientation is close to transverse (e.g., the right side of the ($\nabla\mathbf{v}$, $\mathbf{v}$) image and the left side of the ($\mathbf{v}$, $\nabla\times\mathbf{v}$) image).

At point B, the 1,3-birefringence indicates that the transverse population is at its maximum. In a sense, this represents the strongest bimodal character (parallel-transverse) that the system ever passes through on its way to parallel alignment. However, the texture at this point does not correspond to the "kink band" texture (sharp tilt boundaries between parallel regions and transverse bands) that is observed in the analogous bimodal distribution in a much higher molecular weight lamellar diblock (PS-PEP 40k−70k).[20] Instead, there are transverse domains coexisting with poorly organized regions and with overall parallel regions containing chevron bands. This is reminiscent of the texture of transverse islands in a matrix of parallel material reported by Hudson for a lamellar diblock sheared in this regime ($\omega \gg \omega_c'$).[21]

Point C along the Parallel Alignment Trajectory Far above ω_c'. During the first part of the slow process, the transverse projection is distinctly reduced, while the parallel projection is strongly enriched (Figure 17). The drop in the transverse component correlates with the reduced magnitude of the negative 1,3-birefringence at point C relative to B (Figure 14b). TEM images show that essentially all of the material is now well organized into layers. The characteristic chevron pattern of defects dominates the images in the ($\nabla\mathbf{v}$, $\mathbf{v}$) plane, but with a length scale that is dramatically longer than was evident at point B along this trajectory. The images in the ($\nabla\mathbf{v}$, $\nabla\times\mathbf{v}$) and ($\mathbf{v}$, $\nabla\times\mathbf{v}$) planes accord with predominant parallel alignment.

Note that this state of alignment corresponds roughly to the midpoint in the slow process; we do not regard it as a well-aligned state. Samples taken after the 1,3-birefringence has returned to zero show much narrower SAXS peaks[19] and no longer show tilt boundaries in TEM images (a representative image is shown in Figure 13).

By comparison of the degree of alignment at roughly the middle of the slow process (point C) for each of the three trajectories, it is clear that the uniformity of orientation increases as one moves to higher frequency regimes. This qualitative trend agrees with previous descriptions of final states of alignment in PEP−PEE[7] and PS−PI[9,10] lamellar melts.

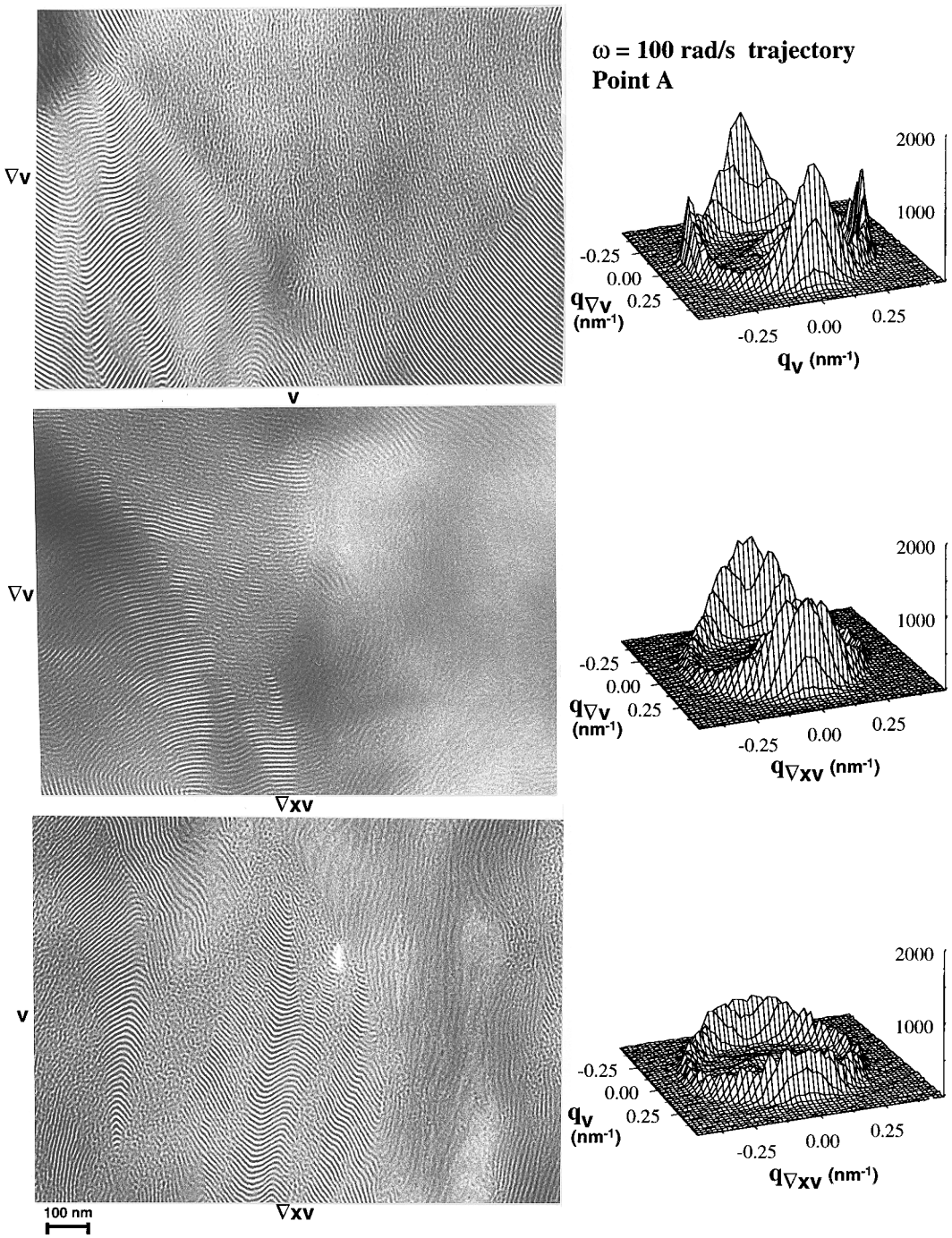

Figure 15. Structure at point A along the parallel alignment trajectory shown in Figure 14b as revealed by TEM and SAXS. The scale for SAXS intensity can be quantitatively compared to points B and C for this trajectory.

4. Discussion

In the intense effort to understand the physics of flow-induced alignment of lamellar block copolymers, progress toward the goal of determining the mechanisms of alignment has been limited. Dating back to the early work of Keller and Hadziioannou, the concepts of grain rotation, anisotropic viscoelasticity, selective melting, and defect migration have been considered.[2,3,9] Since the discovery of perpendicular alignment, the selective melting hypothesis has taken on a special role in explaining the development of perpendicular alignment under conditions close to the ODT.[7] The idea that the system moves into a configuration that minimizes its modulus has been advocated as the means of selecting one orientation over another.[2,15] It also has to be acknowledged that two or more mechanisms may act in combination to produce alignment.[3,9] However, direct evidence of these mechanisms and their relative importance in flow-induced alignment has been lacking. Consequently, there is insufficient fundamental basis for predicting the direction, degree, and dynamics of the alignment process.

Recent rheo-optical results have provided powerful evidence that during the course of shearing there is a transition in the character of alignment, as though one process overtakes another in importance.[19] Three alignment regimes were established for PS−PI cooled from $T > T_{ODT}$ directly to the temperature at which shear-induced alignment is performed (Figure 2): (I) perpendicular alignment ($\omega < \omega_c'$), (II) parallel alignment via orientation distributions with strong perpendicular and parallel projections ($\omega_c' < \omega < 10\omega_c'$), and (III) parallel alignment via orientation distributions richer in transverse and parallel projections $10\omega_c' < \omega$). The distinct

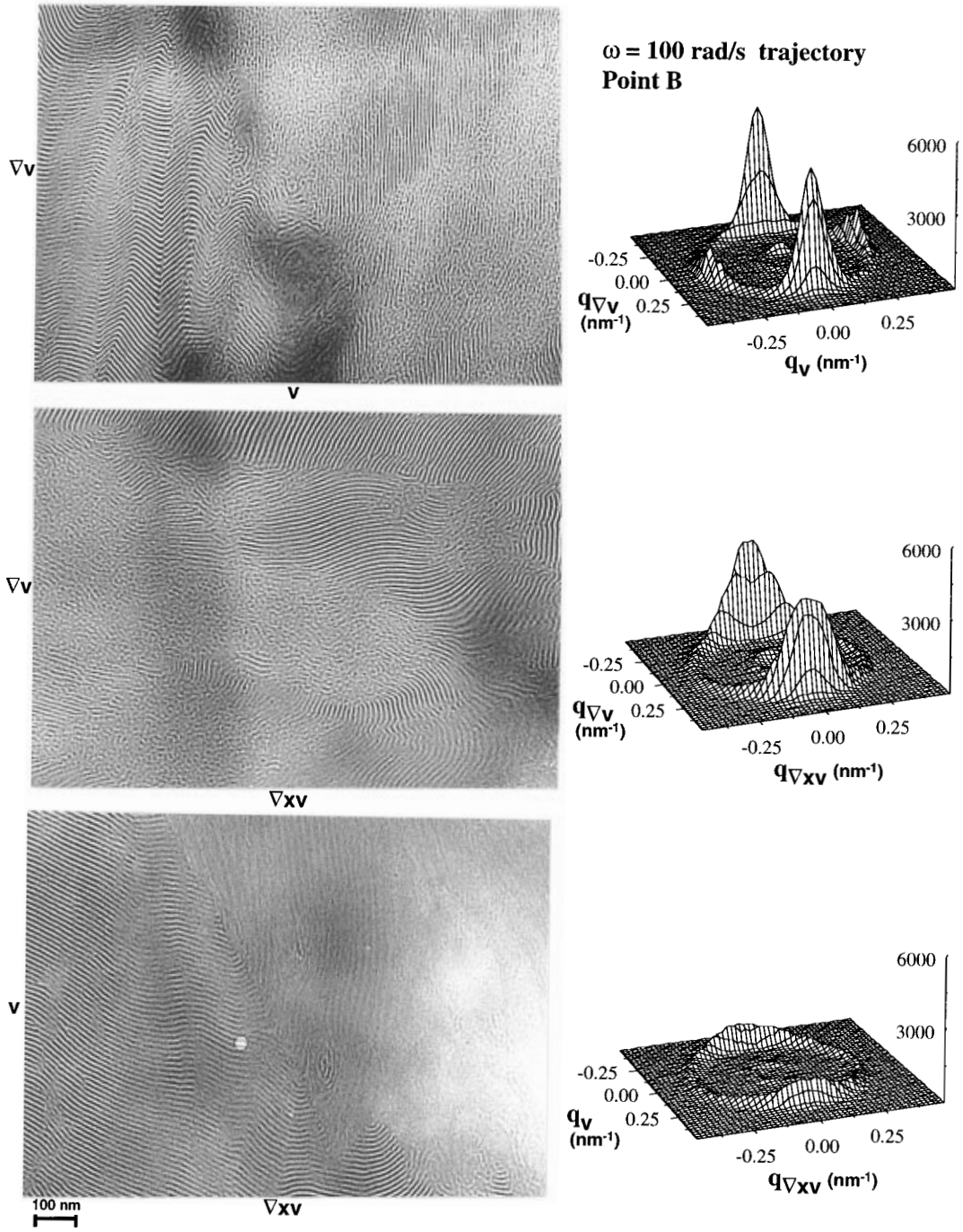

Figure 16. Structure at point B along the parallel alignment trajectory shown in Figure 14b as revealed by TEM and SAXS. The scale for SAXS intensity can be quantitatively compared to points A and C for this trajectory.

strain dependencies of rates of the fast and slow processes and the qualitative difference between the orientations they induce in each of the three regimes strongly suggested that the physics for the distinct processes were different. However, it was not possible to infer from the rheo-optical results what the distinct mechanisms might be.

The present results provide valuable complementary information that may highlight the key physics associated with the fast and slow processes. In particular, the electron micrographs reveal how the texture evolves as one moves through each stage of the three types of alignment trajectories.

A. Evolution of Microstructure. A general feature that emerges from the TEM images is that the fast process of all three trajectories is largely responsible for the formation of layers from poorly organized material. From the SAXS results it is clear that the population of layers that is created is not isotropic—but neither is it unimodal. In general, the orientations that are enhanced in the fast process share a common tangent: for example, the fast processes of trajectory types I and II enhance orientations that have lamellae tangent to the **v** direction, while the fast process of a type (III) trajectory creates layers with edges along $\nabla\times\mathbf{v}$. As the trajectory reaches the transition from the fast to the slow process, a distinctive texture develops for each trajectory: at the end of the fast process in trajectory I the texture viewed in the ($\nabla\mathbf{v}$, $\nabla\times\mathbf{v}$) plane consists of well-organized layered domains separated by bands of poorly organized material; in (II) the layers meander fairly gently in the ($\nabla\mathbf{v}$, $\nabla\times\mathbf{v}$) plane, and in (III) the microstructure viewed in the ($\nabla\mathbf{v}$, **v**) plane includes residual poorly organized regions, transverse domains, and large regions with mean orientation in the parallel direction, which contain tilt walls that are oriented normal to the

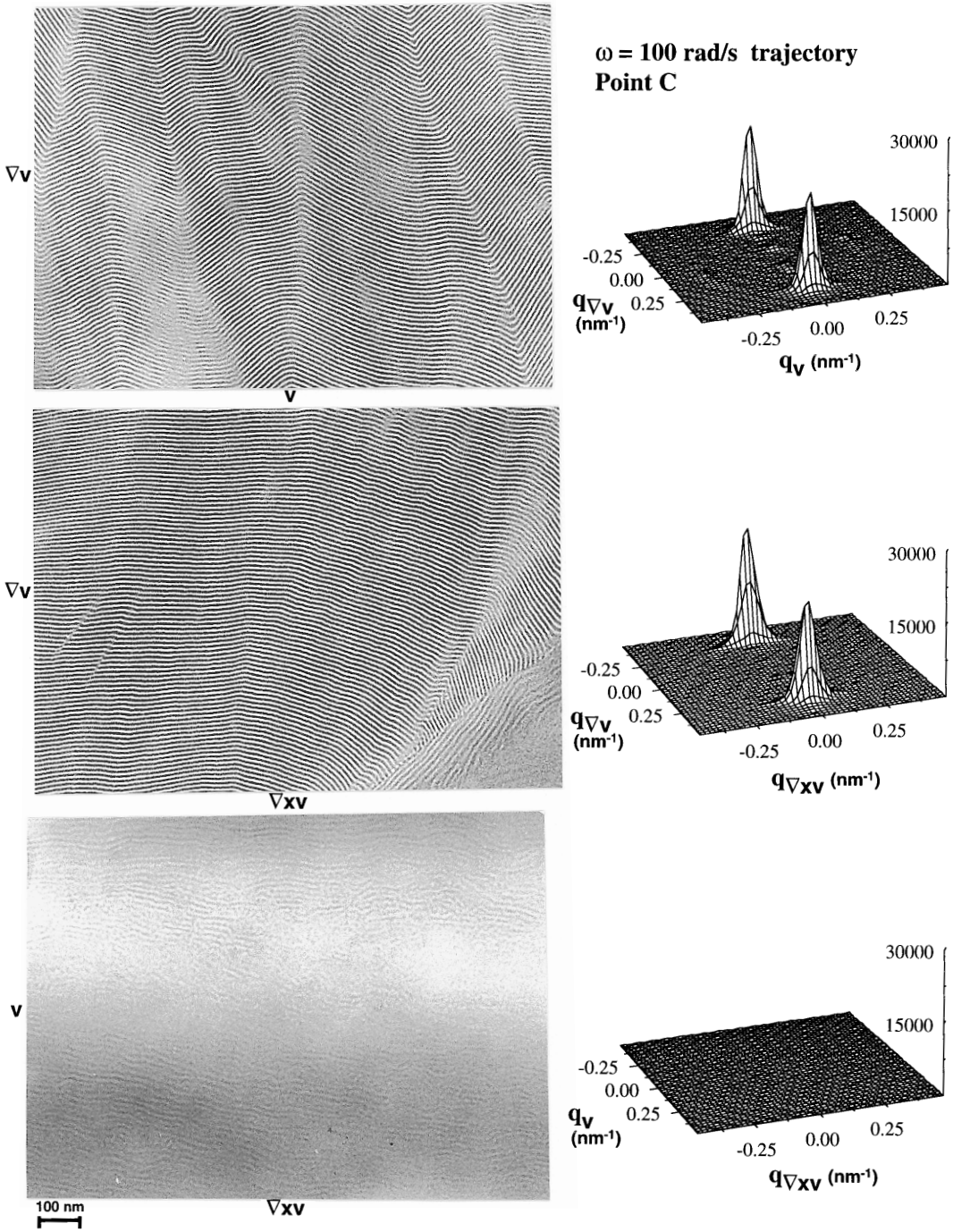

Figure 17. Structure at point C along the parallel alignment trajectory shown in Figure 14b as revealed by TEM and SAXS. The scale for SAXS intensity can be quantitatively compared to points A and B for this trajectory.

flow direction, forming a chevron pattern.

The slow process generally appears to coarsen the structure that exists once most of the material has been converted to well-organized layers; it is during this process that the range of orientations that were enriched during the fast process is selectively winnowed down to a single orientation.

The path to perpendicular alignment (family I, $\omega < \omega_c'$) begins with the enhancement of perpendicular and parallel layers and the orientations in between during the "fast process". While perpendicular layers are enhanced during the whole process, parallel layers are eliminated later. The first half of the slow process is responsible for the elimination of residual bands of poorly organized texture that separate lamellar domains at the end of the fast process. Relatively isolated poorly organized islands seem to persist at the midpoint of the "slow process" even in regions with a strong overall perpendicular alignment.

Like the trajectory to perpendicular alignment, the pathway to parallel alignment at modestly high frequency (family II, $\omega_c' < \omega < 10\omega_c'$) begins with the buildup of perpendicular and parallel layers and the orientations in between. But in this process, the parallel projection grows more quickly than the perpendicular. The subsequent "slow process" narrows the orientational distribution toward parallel alignment by eliminating poorly organized regions and reducing the angular variations associated with the undulating domain texture.

In family III trajectories (very high-frequency route to parallel, $\omega_c' \ll \omega$), the "fast" process transforms poorly organized material to layers that are predominantly aligned along the parallel and transverse direc-

tions, but not along orientations between the two. This is the only one of the three families of trajectories that shows distinctly bimodal transient states. As most of the poorly organized regions are transformed to lamellae, the transition to the "slow" process is marked by the development of a characteristic texture in regions of average orientation along the parallel direction, with bands tilted about the vorticity axis to form chevron patterns. The coarsening of this pattern appears to dominate the slow process, during which the transverse projection is also eliminated. At the end of the slow process a well-aligned "single-crystal-like" state is achieved.

These observations build a much clearer picture of the evolution of shear-induced alignment processes than was previously possible from the transient rheo-optical results that established the families of trajectories or from structural studies that did not have a context for relating the sample points to their corresponding positions along a given alignment trajectory.

B. Implications Regarding Alignment Mechanisms. There are three mechanisms of flow-induced alignment that have been frequently mentioned in the literature: selective melting, defect migration, and grain rotation. Therefore, we first comment on the implications of the TEM and SAXS results regarding the existence and importance of these three mechanisms. Then we comment on a process that is strongly indicated by each sequence of TEM images, but which appears not to have been considered previously: selective *creation* of lamellae from ordered, but poorly organized, material. Finally, some suggestions regarding future theoretical work will be discussed.

From the progression of local structure seen in the TEM images, there is no evidence of selective lamellar melting or flow-induced disordering. This is particularly significant in relation to the perpendicular alignment trajectory, since the selection of perpendicular alignment has been attributed to flow-induced disordering followed by ordering under the influence of shear, which produces perpendicular lamellae. Since melting is most likely to play a role when the amount of unfavorably oriented material is greatest, it would produce a rapid growth of the perpendicular alignment at the early stage of the process, while depleting (or leaving unchanged) other orientations. The observed texture at points A and B and the corresponding orientation distributions indicated by SAXS fail to show evidence of such a highly selective mechanism.

A number of images do suggest that defect migration plays a role, especially in the later stages of the alignment process. One example is the disappearance of the bands of poorly organized material separating well-ordered lamellar domains during parallel alignment close to ω_c' (type II trajectory). This could indicate that the boundary between the two types of regions moves in the direction of the poorly organized material, which disappears when the boundaries on each side meet. An even more compelling example is the coarsening of the chevron texture during parallel alignment at very high frequencies (type III trajectory). If tilt walls on either side of a relatively steeply tilted band moved together and annihilated each other, the process could produce the observed increase in the spacing between and reduction in the misalignment angle across tilt walls that occur between points B and C along this type of trajectory.

Ex-situ methods are not well suited to confirming or negating grain rotation. However, the general observation that extended domains of well-defined lamellae develop as a result of the alignment process suggests that *if* grain rotation plays a role, in the fast process it would correspond to rotation of a domain of well-organized layers within a matrix that has a large amount of poorly organized material and, in the slow process, "grains" that have formed might reorient in a cooperative manner with adjacent regions that are also well-organized, but differently oriented with respect to the flow. To date the most direct evidence of grain rotation comes from the rheo-optical signature of the low frequency ($\omega < \omega_d$) alignment process in a PEP−PEE lamellar diblock.[14] Although such a regime has been reported in specially annealed PS−PI diblocks and in both annealed and unannealed PEP−PEE diblocks, it is not observed in PS−PI that is simply heated through the ODT to erase prior thermal and flow history and then cooled to the shearing temperature. Although it is beyond the scope of the present study, future work on the effects of annealing on the trajectories of alignment in PS−PI at very low frequency may provide additional information on the role of grain rotation in producing the low-frequency pathway to parallel alignment.

In all three trajectories explored here, shearing appears to play a role in converting poorly organized material into well-defined lamellae. The selectivity of this reorganization process appears to direct the initial development of the orientation distribution during the fast process. The reorganization process has a particularly interesting feature in the very high-frequency regime: it produces mainly parallel and transverse lamellae.

Bimodal transverse-parallel distributions have been attributed to entanglement and strong segregation.[22] In addition, it has been asserted that parallel alignment is simply controlled by the loss tangent, implying that one type of trajectory applies to all routes to parallel alignment.[24] The present results indicate that these bimodal distributions also occur in nonentangled polymers and in weak segregation, and that they correspond to type III trajectories to parallel alignment ($\omega \gg \omega_c'$), but not to type II trajectories to parallel alignment ($\omega_c' < \omega < 10\omega_c'$). As to the mechanism responsible for the bimodal distribution, the creation of transverse domains has been attributed to alignment of entangled chains along the flow direction. However, this is unlikely to be an adequate explanation, since the bimodal distribution can occur at small strain amplitudes (as small as $\gamma_o = 0.1$) in both entangled and unentangled systems. At small strain amplitudes, segmental orientation is hardly perturbed, and its orientation is along the extensional axis of the shear (45° with respect to the flow direction). Thus, a more general explanation is needed. We have presented a mechanism that overcomes these deficiencies and applies to a wide range of systems so long as $\omega \gg \omega_c'$.[41] This explanation requires only a symmetry argument and the distortion of chain conformation to explain the simultaneous creation of both transverse and parallel orientations during the fast process.

As has been previously noted, the theoretical literature is mainly devoted to the relative stability of monodomains with different orientation with respect to the flow geometry.[5,6,13,31,32] Since the rate, degree, and direction of alignment are determined by the way the orientation distribution evolves dynamically from the complex initial texture to a well-aligned material, consideration of the stability of the ultimate microstructure alone is not enough. Guided by the TEM and SAXS results, it may be possible to break the overall alignment

process into parts that are tractable by analysis or simulation. For example, the conversion of poorly organized material into lamellae might be treated as an individual part; future work might examine how this reorganization proceeds at very high frequencies where chain dynamics may play an important role and contrast this high-frequency process with the reorganization into lamellae at low frequencies where nanostructural dynamics, including fluctuations, dominate the flow behavior. The TEM images also suggest specific types of defect migration that might be investigated theoretically. For example, in the very high frequency regime, the evolution of chevron patterns of defects under the influence of oscillatory shear might be tractable, giving insight into the slow process of the type III trajectories to parallel alignment. The new information on the evolution of microstructure at well-defined stages in the alignment process may present opportunities in modeling and simulation, which in turn could yield valuable insights to guide the unified design of materials and processing conditions to exploit flow-induced alignment.

5. Conclusion

The combination of real-time in-situ rheo-optical methods with ex-situ small angle X-ray scattering and transmission electron microscopy for nano-, micro-, and macroscopic observations reveals the structural evolution during flow-induced alignment of a model diblock copolymer through different trajectories. By spanning the range of length and time scales involved, we can observe the cascade of structural changes: the formation of layers from poorly organized regions; the creation, growth, coarsening, and deformation of domains; the generation and elimination of defects; and the perfection of well-aligned "single-crystal-like" order. These results enable us to re-evaluate numerous proposed mechanisms of block copolymer alignment that have been put forward over the past two decades.[2−32] For example, in the PS−PI system, we find no evidence of selective melting or flow-induced disordering; instead, results suggest selective creation of well-defined lamellae from poorly organized regions, particularly in the initial fast processes of various alignment trajectories. Observations of different types of defects and their anisotropic arrangement during the fast and slow processes of each trajectory make the general concept of defect dynamics more specific in terms of both the type of defects involved and the dynamic regime where they are important. For example, partially formed focal conic defects appear in the initial ordered, but unaligned, block copolymer lamellae and disappear during the fast processes of each trajectory. In the slow process of each trajectory the majority of the material exists in well-defined layers and these form different types of defects in each of the three trajectories, as described above.

Recently, shear-induced parallel-transverse orientation distributions have been observed in disparate systems.[21,22,29,30] This surprising texture has attracted considerable interest. It has been asserted that this type of structure is characteristic of parallel alignment of strongly segregated, entangled polymers.[22] However, the present results show that this type of microstructure, manifested by four-spot scattering patterns in the ($\mathbf{v}$, $\nabla\mathbf{v}$) plane, is particular to the very high frequency regime and occurs in both unentangled and entangled polymers in both weakly and strongly segregated states. Indeed, the common feature of all reports of the parallel-transverse bimodal structure is that the materials were subjected to oscillatory shearing in the very high frequency regime ($\omega_c' \ll \omega$). From this insight, we have suggested a mechanism for simultaneous creation of transverse and parallel lamellae in the fast process of the high-frequency trajectory to parallel alignment.[41] This mechanism invokes only symmetry arguments and the role of conformational distortion of the chains when subjected to rapid deformations.

Information on the microstructural nature of the initial fast process and subsequent slow process of each trajectory provides greater insight into the distinct physics involved in each of the three alignment regimes. In turn, more specific physical concepts may provide a guide for modeling and simulation of dynamic processes during shear: it appears reasonable to break each type of trajectory down into processes that dominate at different stages (e.g., early vs late), which could be integrated together to describe the whole alignment trajectory. Based on the success of this experimental approach in clarifying the dynamics of the present lamellar diblock, it is being extended to other nanostructures, including various diblock copolymers and the elaborate structures formed by ABC triblock copolymers. The combination of rapid in-situ measurements with detailed ex-situ structural characterization has the potential to uncover the physics of flow-induced alignment in a wide range of self-assembled materials.

Acknowledgment. This research was carried out with the support of the NSF-CTS 9421015, AFOSR-Liquid Crystals MURI, Chevron and Raychem. We thank Hans Spiess and Uli Wiesner for inspiring this work; Glenn Fredrickson, Scott Milner, Zhen-Gang Wang, Ron Larson, Frank Bates, Karen Winey, and Nitash Balsara for insightful discussions; and Richard Spontak, Steve Hudson, and Faith Morrison for valuable feedback on the manuscript.

References and Notes

(1) Keller, A.; Pedemonte, E.; Willmouth, F. M. *Colloid Polym. Sci.* **1970**, *238*, 25. Folkes, M. J.; Keller, A.; Scalisi, F. P. *Colloid Polym. Sci.* **1973**, *251*, 1.
(2) Hadziioannou, G.; Mathis, A.; Skoulious, A. *Colloid Polym. Sci.* **1979**, *257*, 136. Hadziioannou, G.; Mathis, A.; Skoulious, A. *Macromolecules* **1982**, *15*, 258.
(3) Morrison, F. A.; Winter, H. H. *Macromolecules* **1989**, *22*, 3533. Morrison, F. A.; Winter, H. H.; Gronski, W.; Barnes, J. D. *Macromolecules* **1990**, *23*, 4200.
(4) Bates, F. S.; Fredrickson, G. H. *Annu. Rev. Phys. Chem.* **1990**, *41*, 525. Bates, F. S. *Science* **1991**, *251*, 898. Bates, F. S.; Fredrickson, G. H. *Annu. Rev. Mater. Sci.* **1996**, *26*, 501. Colby, R. H. *Curr. Opin. Colloid Interface Sci.* **1996**, *1*, 454.
(5) Cates, M. E.; Milner, S. T. *Phys. Rev. Lett.* **1989**, *62*, 1856. Bruinsma, R.; Rabin, Y. *Phys. Rev. A* **1992**, *45*, 994. Goualian, M.; Milner, S. T. *Phys. Rev. Lett.* **1995**, *74*, 1775.
(6) Fredrickson, G. H. *J. Rheol.* **1994**, *38*, 1045.
(7) Koppi, K.; Tirrel, M.; Bates, F. S.; Almdal, K.; Colby, R. H. *J. Phys. II* **1992**, *2*, 1941.
(8) Koppi, K.; Tirrel, M.; Bates, F. S. *Phys. Rev. Lett.* **1993**, *70*, 1449.
(9) Winey, K. I.; Patel, S. S.; Larson, R. G.; Watanabe, H. *Macromolecules* **1993**, *26*, 2542.
(10) Winey, K. I.; Patel, S. S.; Larson, R. G.; Watanabe, H. *Macromolecules* **1993**, *26*, 4373.
(11) Larson, R. G.; Winey, K. I.; Patel, S. S.; Watanabe, H. *Rheol. Acta* **1993**, *32*, 245.
(12) Riise, B. L.; Fredrickson, G. H.; Larson, R. G.; Pearson, D. S. *Macromolecules* **1995**, *28*, 7653.
(13) Amundson, K.; Helfand, E.; Quan, X.; Hudson, S. D.; Smith, S. D. *Macromolecules* **1994**, *27*, 6559.
(14) Kannan, R. M.; Kornfield, J. A. *Macromolecules* **1994**, *27*, 1177.
(15) Patel, S. S.; Larson, R. G.; Winey, K. I.; Watanabe, H. *Macromolecules* **1995**, *28*, 4313.
(16) Zhang, Y.; Wiesner, U.; Spiess, H. W. *Macromolecules* **1995**, *28*, 778.
(17) Gupta, V. K.; Krishnamoorti, R.; Kornfield, J. A.; Smith, S. D. *Macromolecules* **1996**, *29*, 1359.
(18) Gupta, V. K.; Krishnamoorti, R.; Kornfield, J. A.; Smith, S. D. *Macromolecules* **1995**, *28*, 4464.

(19) Gupta, V. K.; Krishnamoorti, R.; Chen, Z.-R.; Kornfield, J. A.; Smith, S. D.; Satkowski, M. M.; Grothaus, J. T. *Macromolecules* **1996**, *29*, 875.
(20) Polis, D. L.; Winey, K. I. *Macromolecules* **1996**, *29*, 8180.
(21) Hudson, S. D.; Amundson, K. R.; Jeon, H. G.; Smith, S. D. *Mater. Res. Soc. Bull.* **1995**, *20*, 42.
(22) Zhang, Y. M.; Wiesner, U. *J. Chem. Phys.* **1995**, *103*, 4784.
(23) Zhang, Y.; Wiesner, U.; Yang, Y.; Pakula, T.; Spiess, H. W. *Macromolecules* **1996**, *29*, 5427.
(24) Zhang, Y.; Wiesner, U. *J. Chem. Phys.* **1997**, *106*, 2961.
(25) Morrison, F. A.; Mays, J. W.; Muthukumar, M.; Nakatani, A. I.; Han, C. C. *Macromolecules* **1993**, *26*, 5271.
(26) Nakatani, A. I.; Morrison, F. A.; Douglas, J. F.; Mays, J. W.; Jackson, C. L.; Muthukumar, M.; Han, C. C. *J. Chem. Phys.* **1996**, *104*, 1589.
(27) Balsara, N.; Hammouda, B.; Kesani, P. K.; Jonnalagadda, S. V.; Straty, G. C. *Macromolecules* **1994**, *27*, 2566. Balsara, N. P.; Hammouda, B. *Phys. Rev. Lett* **1994**, *72*, 360.
(28) Wang, H.; Kesani, P. K.; Balsara, N. P.; Hammouda, B. *Macromolecules* **1997**, *30*, 982.
(29) Pinheiro, B. S.; Hajduk, D. A.; Gruner, S. M.; Winey, K. I. *Macromolecules* **1996**, *29*, 1482.
(30) Okamoto, S.; Saijo, K.; Hashimoto, T. *Macromolecules* **1994**, *27*, 5547.
(31) Amundson, K.; Helfand, E.; Davis, D. D.; Quan, X.; Patel, S. S.; Smith, S. D. *Macromolecules* **1991**, *24*, 6546. Amundson, K.; Helfand, E.; Quan, X.; Smith, S. D. *Macromolecules* **1993**, *26*, 2698.
(32) Amundson, K.; Helfand, E. *Macromolecules* **1993**, *26*, 1324.
(33) The rheo-optical results presented here and in our earlier papers[17−19] are from the same batch of PS−PI. In the previous studies only one aliquot from this batch was used for a whole suite of rheo-optical experiments. Here various samples are loaded, processed, and removed for ex-situ characterization; therefore a series of aliquots from the same batch of polymer are used. Since small variations in the ODT were previously detected from aliquot to aliquot taken from the same batch of polymer,[18,19,34] rheo-optical characterization of each loading was used to confirm that it behaved in accord with all other samples in the series.
(34) We performed a temperature sweep at a rate of 1 °C/min and in steps of 1 °C. At each temperature the dynamic moduli were measured using oscillatory shear at 10 rad/s and 2% strain. At T_{ODT}, both G' and G'' exhibited a steep decrease, which was more pronounced for G'. Similar determination revealed a typical hysteresis behavior upon cooling with the transition temperature a few degrees lower than that during heating. For yet unknown reasons, we observed T_{ODT} ranging from 172 to 164 °C for different aliquots of the same polymer batch. All ten aliquots used for the experiments reported in this paper had ODTs between 170 and 172 °C.
(35) Kannan, R. M.; Kornfield, J. A. *Rheol. Acta* **1992**, *31*, 535. Kannan, R. M.; Kornfield, J. A.; Schwenk, N.; Boeffel, C. *Macromolecules* **1993**, *26*, 2050.
(36) Lodge, T. P.; Fredrickson, G. H. *Macromolecules* **1992**, *25*, 5643.
(37) Allan, P.; Arridge, R. G. C.; Ehtaiatkar, F.; Folkes, M. J. *J. Phys. D: Appl. Phys.* **1991**, *24*, 1381.
(38) It has been suggested that under certain flow conditions the intrinsic birefringence could dominate over the form birefringence in the present PS−PI,[24] since the theoretical basis for expecting the form contribution to dominate[36] gives a form birefringence that is only approximately 3 times the intrinsic birefringence and is based on a static sample. However, experimental evidence indicates that the form effect is over an order of magnitude larger than the intrinsic birefringence even during shearing. One piece of evidence comes from comparison to a system in which the intrinsic birefringence is known to dominate: PEP−PEE.[14] In this system the intrinsic contributions of the two blocks reinforce each other, whereas the two tend to cancel each other in PS−PI. This trend holds for both flow-induced anisotropy and anisotropy associated with the tendency of chains to align normal to lamellar interfaces. Thus, the birefringence of PEP−PEE tends to provide an upper bound on the intrinsic contribution to the birefringence in PS−PI. The 1,3-birefringence of well-aligned perpendicular PEP−PEE is less than $^1/_{20}$th as large as that of similarly aligned PS−PI; this suggests that the intrinsic component of the birefringence of PS−PI is less than 5% of its form birefringence. Another piece of evidence comes from the magnitude of the birefringence that can be attributed to flow-induced segmental anisotropy. Since the oscillatory stress has a similar amplitude throughout the alignment processes,[18] the stress-induced intrinsic contribution to the displacement of the 1,3-birefringence $\Delta n_{13}^{(d)}$ must remain of the same order of magnitude through the process. Its magnitude can be inferred by the value of $\Delta n_{13}^{(d)}$ observed during shearing when the sample is well aligned: at the conclusion of the alignment process this value is less than 0.1% of the magnitude of $\Delta n_{13}^{(d)}$ observed during the transient stages of the process (see ref 19, Figure 4a for γ_o of 0.9 and 1.0 and Figure 6a for γ_o of 0.6; and in this article see Figure 9b for $\gamma_o = 1.1$ and Figure 14b for $\gamma_o = 0.5$ and 0.7). This suggests that the flow-induced anisotropy of the chains produces a 1,3-birefringence contribution that has a magnitude less than $^1/_{1000}$th of the form birefringence associated with the evolution of the lamellar orientation distribution.
(39) To evaluate the effect of equilibration time on the initial state, we examined TEM micrographs of a sample that was annealed at 115 °C for 24 h and compared them with TEM micrographs of a sample that was annealed for 15 min (see Figure 4). Surprisingly, almost no difference was found in terms of their textures, morphologies, and percentages of poorly organized material. We observed that annealing time did not change the alignment trajectory. A small effect can be detected in the rate of orientation, with longer annealing times producing slightly faster alignment.
(40) Chen, Z.-R.; et al. Unpublished results.
(41) Chen, Z.-R.; Kornfield, J. A.; Smith, S. D.; Grothaus, J. T.; Satkowski, M. M. *Science* **1997**, *277*, 1248.

MA9706743